The meteorological nature of variable soluble iron transport and deposition within the North Atlantic Ocean basin

Walter J. Moxim,[1] Song-Miao Fan,[1] and Hiram Levy II[1]

[1] Aerosol transport from the Sahara desert to the North Atlantic Ocean generates the largest annual flux of mineral dust and total Fe found in the global oceans, enriching the mixed layer with soluble iron. We use the Geophysical Fluid Dynamics Laboratory Global Chemical Transport model to examine the transport and deposition of bioavailable iron on time scales ranging from seasonal to daily. The model is compared with observed mineral dust concentrations, depositions, and soluble Fe fractions. It is shown that simulated cumulative soluble Fe deposition (SFeD) employing a variable Fe solubility parameterization compares well with observed short-term changes of dissolved iron within a thermally stratified surface mixed layer, while assuming a constant 2% solubility does not. The largest year-to-year variability of seasonal SFeD (45 to 90%) occurs throughout winter and spring in the central and northeast Atlantic Ocean. It is strongly linked to the North Atlantic Oscillation (NAO) index, producing substantially more SFeD during the positive phase than the negative phase. The ratio of wet to total SFeD increases with distance from the Saharan source region and is especially large when concentrations are small during the negative NAO. In summer, the relatively steady circulation around the Azores high results in low interannual variability of SFeD (<30%); however, regional short-term events are found to be highly episodic, and daily deposition rates can be a factor of 4 or more higher than the monthly mean flux. Three-dimensional backward trajectories are used to determine the origin and evolution of a specific SFeD event. We show that the dust mass-mean sedimentation rate should be incorporated into the air parcel dynamical vertical velocity for a more precise transport path.

1. Introduction

[2] The micronutrient iron plays an important role in the chemical processes of photosynthesis and nitrogen fixation within the ocean's euphotic zone [*Falkowski et al.*, 1998; *Morel and Price*, 2003] and consequently affects the primary production of phytoplankton and eventual carbon export to the deep ocean. Fresh iron enters the surface mixed layer by upwelling, by entrainment or mixing from below, or by deposition of mineral dust from the atmosphere [*Fung et al.*, 2000; *Jickells et al.*, 2005]. Ocean biogeochemical models dynamically compute ocean iron fluxes, while the atmospheric iron forcing is externally provided by climatological mineral dust deposition fields generated by atmospheric transport models [e.g., *Tegen and Fung*, 1994; *Ginoux et al.*, 2001; *Gao et al.*, 2003; *Luo et al.*, 2003], from which the iron content is assumed (~3.5%) [*Duce and Tindale*, 1991] and a constant iron solubility (1–10%) is prescribed [e.g., *Christian et al.*, 2002; *Gregg et al.*, 2003; *Moore et al.*,

2004; *Vichi et al.*, 2007]. Global observations, although sparse, have shown that Fe solubility is not constant. Measurements of Fe solubility are difficult, with many contrasting techniques; however, they do indicate large geographic variability, with higher solubilities found in areas remote from dust source regions (Table 1). Also, high solubility is often associated with low concentrations [*Chen and Siefert*, 2004; *Baker et al.*, 2006a], indicative of long-range transport.

[3] The solubility measurements suggest some form of atmospheric processing with time. It is known that aerosol iron is found in the form of ferric (hydro)oxides and in other mineral phases such as feldspar and silicates [*Lafon et al.*, 2004]. Iron in the matrices of clay minerals is less readily released than that in ferric oxides because dissolution of clay minerals is generally slower; however, the mechanism for dust iron dissolution during atmospheric transport remains uncertain [*Mahowald et al.*, 2005]. Various mechanisms involving solar radiation, cloud processing, and pollution have been proposed [e.g., *Meskhidze et al.*, 2003; *Hand et al.*, 2004; *Luo et al.*, 2005; *Fan et al.*, 2006]. *Luo et al.* [2005] used a chemical transport model to statistically compare different processes capable of converting insoluble iron to soluble iron with observations of solubility and found that cloud processing and SO_2 in combination agreed best with

---

[1]Geophysical Fluid Dynamics Laboratory, NOAA, Princeton University, Princeton, New Jersey, USA.

Table 1. Measurements of Dust Fe Solubility in Aerosols and Precipitation Defined as the Ratio of Dissolved Fe Passing Through 0.4 μm Pore Size Filters to Total Fe Concentration in a Sample and Model Results[a]

Location	Date	Number of Samples	Sol Fe (%) Obs	Soluble Fe (%) Model	References[b]
		Rain and Snow			
NE Mediterranean (Turkey)	Feb 1996–Jun 1997	87	10	7	1
NW Mediterranean (Tour du Valat)	1988–1989	45	11	9	2
Brittany, France	Sep and Nov	6	17	14	3
North Carolina, USA	Jul 1997–Jun 1999	81	26	19	4
Antarctica	Aug-Dec	31	32 (9–89)	20	5
Summit, Greenland	Ice core	17	40 (10–60)	20	6
Bermuda Island	Mar	4	16	11	7
Bermuda Island	Aug	12	48	16	7
Rhode Island, USA	Apr	3	16	18	8
Rhode Island, USA	May	1	20	20	8
Rhode Island, USA	Jul	4	17	26	8
Pacific Islands	Apr	1	21	23	8
Pacific Islands	Oct	1	12	29	8
N. E. Pacific	May	1	23	15	8
		Aerosols			
Pacific cruise, 25°N	Apr 2001	18	2	16	9
Pacific cruise, 25°N	May 2002	25	10	21	10
Pacific Islands	Jan-Oct	27	56 ± 32	27	11
Atlantic cruise, 26°N	Jan-Feb 2001	7	32	15	12
Atlantic cruise, 15°N	Jan-Feb 2001	23	5	3	12
Atlantic cruise, 15°N	Jul-Aug 2001	6	3	4	12
Atlantic cruise, 5°N	Jul-Aug 2001	24	5	4	12
Atlantic cruise (49°N–25°N)	Sep 2001–Oct 2002	17	15 (2–54)	13 (4–49)	13
Atlantic cruise (21°N–6°N)	Oct 2000, Sep 2001	6	8 (2–25)	4 (3–16)	13
Barbados (13°N)	Sep 1992	25	6	5	14
Barbados (13°N)	Sep 2007	29	1–3	5	15
Atlantic cruise (10°N)	Oct-Nov 2002	16	1	1, 3	16
Atlantic cruise (1°N–11°S)	Oct 2000, Oct 2001	10	10 (4–24)	21 (13–24)	13
Atlantic cruise (16°S–42°S)	Oct 2001	9	10 (4–24)	15 (1–22)	13

[a]Note that 1-2% of particulate Fe may pass through.

[b]References are numbered as follows: 1, *Ozsoy and Saydam* [2001]; 2, *Guieu et al.* [1997]; 3, *Colin et al.* [1990]; 4, *Kieber et al.* [2001]; 5, *Edwards and Sedwick* [2001]; 6, *Laj et al.* [1997]; 7, *Kieber et al.* [2003]; 8, *Zhuang et al.* [1992b]; 9, *Hand et al.* [2004]; 10, *Buck et al.* [2006]; 11, *Zhuang et al.* [1992a]; 12, *Chen and Siefert* [2004]; 13, *Baker et al.* [2006a]; 14, *Zhu et al.* [1997]; 15, *Trapp et al.* [2010]; 16, *Baker et al.* [2006b].

observed soluble Fe. *Fan et al.* [2006] developed a parameterization in the Geophysical Fluid Dynamics Laboratory (GFDL) Global Chemical Transport model (GCTM) that utilized a mechanism converting dust from fresh to acid-coated aerosols by heterogeneous chemistry and cloud processing, followed by dissolution of iron minerals into the aqueous coating. They chose to model iron dissolution following the mechanism proposed by *Zhuang et al.* [1992a], which invokes three processes: (1) Dust particles are incorporated into cloud water, (2) SO_2 dissolves in cloud water and is oxidized to produce sulfuric acid, and (3) cloud droplets evaporate. Dust particles are left with a soluble coating of sulfate and other salts. When sulfuric acid is the main component, the coating is strongly acidic. The dissolution of hematite and goethite increases rapidly with acidity, as does the solubility of ferric hydroxide in aqueous solution. The model qualitatively captured the observed gradients of soluble iron.

[4] The evidence of variable Fe solubility as indicated by measurements and the subsequent increase in simulated soluble Fe deposition (SFeD) over the remote ocean [*Fan et al.*, 2006] implies a significant correction to the atmospheric iron deposition currently used by ocean biogeochemistry models. This is likely to alter the simulated iron cycling and associated dissolved iron (dFe) in the upper ocean, and the effect should be seen over timescales ranging

from annually to daily. It has been shown that the daily variability of mineral dust deposition within 1 month is much larger than the variability in monthly means over different years [*Mahowald et al.*, 2003; *Aumont et al.*, 2008] and that 30–90% of the annual averaged dust deposition is produced on just 5% of the days in a year [*Mahowald et al.*, 2009]. This in turn implies that SFeD actually occurs in short-term, high-magnitude episodes rather than at the monthly mean SFeD rate used in most ocean biogeochemistry models.

[5] While mineral dust deposition has been observed and analyzed over timescales ranging from annually to daily, less is known of the meteorological transport driving its magnitude and variability. This study investigates the meteorological aspects of seasonal and episodic SFeD within the North Atlantic Ocean basin, which receives large yearly amounts of transported mineral dust because of its proximity to the Sahara Desert [*Prospero*, 1996]. The analysis is based on data generated by the GFDL GCTM utilizing the variable soluble iron parameterization scheme developed and used in earlier studies [*Fan et al.*, 2004; *Fan et al.*, 2006; *Cassar et al.*, 2008] and described in section 2. Of particular note, the model has previously demonstrated that the association of lower concentrations with high solubility as a function of transport time produces considerably more annual SFeD to the remote ocean than assuming a
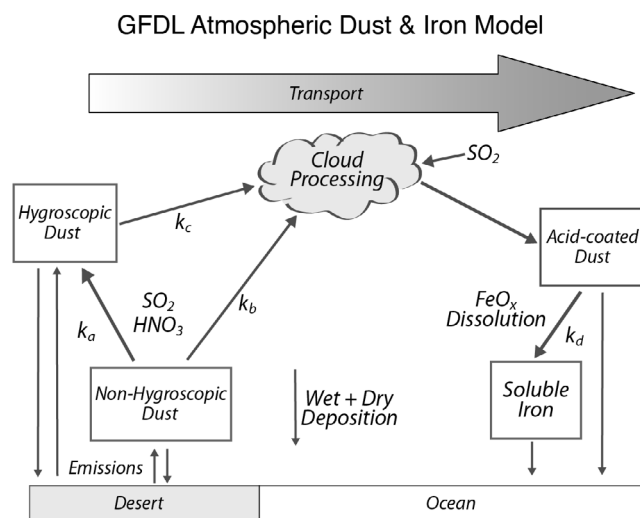
GFDL Atmospheric Dust & Iron Model

Figure 1. A schematic box diagram of model mineral dust evolution from freshly emitted to bioavailable soluble iron. k_a, k_b, k_c, and k_d correspond to the rate coefficients described in section 2.

constant (5%) solubility [*Fan et al.*, 2006]. Variable solubility is employed throughout the rest of this study, and its importance is reemphasized in section 3.4.

[6] The paper is organized as follows. Section 2 contains the model description. Section 3 provides a comparison with available observations of mineral dust concentration and deposition, as well as soluble Fe fractions. Additionally, measurements of local short-term changes in mixed layer dFe provided by selected cruises are evaluated against model cumulative SFeD. Section 4 describes the meteorology driving the year-to-year variability and magnitude of SFeD and mineral dust transport on timescales ranging from seasonal to monthly. The role of the North Atlantic Oscillation (NAO) index during winter and spring is emphasized, and an analysis of an observed summer synoptic scale mineral dust and SFeD event in the Sargasso Sea is discussed in detail. Section 5 contrasts the regional monthly mean bioavailable soluble Fe flux rates into the ocean mixed layer with episodic daily rates, and section 6 summarizes the study.

2. Model Description

[7] The original GFDL GCTM [*Mahlman and Moxim*, 1978] was adapted to use National Centers for Environmental Prediction (NCEP) reanalysis winds, archived every 6 h, on the same 28 vertical (sigma) levels [*Kalnay*, 1996]. The u and v components of the horizontal NCEP winds were linearly interpolated to the GCTM equal area 265 km horizontal grid, which has effective longitude-latitude resolutions of 2.4° × 2.4° in the tropics and 3°–3.5° × 2.4° in midlatitudes. The vertical velocities are calculated online from the horizontal mass divergence and the surface pressure tendency.

[8] Subgrid scale vertical mixing is parameterized by a diffusion coefficient (K_z) [*Levy et al.*, 1982]. In the surface mixed layer, K_z is calculated from the surface momentum

flux and vertical wind shear, both of which are derived from the NCEP reanalyses using an approximation that momentum flux is constant with altitude [*Zhang and Anthes*, 1982]. The boundary layer height is diagnosed from the bulk Richardson number. Vertical transport by deep convection is parameterized as lifting an ensemble of air masses from the boundary layer to the top of convection as determined from the moist Richardson number [*Levy et al.*, 1982] and a layer-by-layer downward redistribution of air to represent subsidence and maintain mass balance. The amount of air lifted (per horizontal grid per 6 h) is calculated from the difference of saturation humidity between the bottom and top layers in the convective column and the grid scale average precipitation. Grid scale advection is calculated using a finite difference scheme [*Mahlman and Moxim*, 1978]. The advection time step is 26 min, and the vertical diffusion time step is 2.6 min.

[9] Dust entrainment flux (F; in kg m^{-2} s^{-1}) is predicted in the model from surface friction velocity (u^*, m s^{-1}, derived from the surface momentum flux) as follows [*Marticorena and Bergametti*, 1995]:

$$F = C\,\mathbf{S}(x,y)(u^* + u_t^*)\left(u^{*2} - u_t^{*2}\right), \qquad (1)$$

where C is a scaling factor (= 0.003 kg m^{-5} s^2), $\mathbf{S}(x, y)$ is a function of longitude (x) and latitude (y) that specifies the spatial distribution of dust sources taken from *Ginoux et al.* [2001], and u^*_t is a threshold of u^* below which there is no entrainment. The $\mathbf{S}(x, y)$ function has implicitly incorporated factors such as vegetation cover, soil texture, and erosion surface area and was guided by topography and multiyear satellite observations of dust aerosols [*Prospero et al.*, 2002]. The original $\mathbf{S}(x, y)$ is doubled in the Taklimakan and Gobi deserts to increase model dust concentrations at Asian sites. The magnitude of u^*_t depends on soil moisture [*Fecan et al.*, 1999] and surface roughness [*Raupach et al.*, 1993; *Marticorena and Bergametti*, 1995]. However, we choose to use u^*_t = 0.35 m s^{-1} everywhere on the basis of a lack of accurate spatial data on surface soil moisture and roughness and grain size distribution. Dust emission is suppressed for 24 h after the occurrence of grid box precipitation.

[10] The GCTM calculates three life stages for mineral dust evolution: freshly emitted, acid coated, and finally the mass of bioavailable soluble Fe (Figure 1). This is accomplished by transporting four types of tracers distributed in four bin sizes (0.1–1, 1–1.8, 1.8–3, 3–6 μm in radius): mobilized fresh "nonhygroscopic" dust particles that are removed by precipitating ice clouds, but not by water clouds; mobilized fresh hygroscopic dust particles that are removed by both precipitating ice and water clouds, acid-coated dust particles; and the mass of soluble Fe from mineral Fe (FeO$_x$) dissolution of the acid-coated dust particles. Soluble Fe attributed to combustion sources is not included. The work by *Luo et al.* [2008] demonstrated that combustion sources are not important contributors to iron deposition in the open oceans, supplying less than 5% of the total deposition.

[11] As depicted in the schematic box diagram in Figure 1, mineral dust is emitted as fresh particles. While recent studies have suggested that a fraction of Saharan dust may be removed by both ice and water clouds, the actual ratios are not

known [e.g., *Twohy and Anderson*, 2008; *Twohy et al.*, 2009]. For this study, fresh nonhygroscopic Saharan dust particles are assumed to be removed by ice clouds and/or converted to a form that is removed by water clouds through surface chemical reactions with HNO_3 and SO_2 molecules [*Dentener et al.*, 1996]. We utilize simulated monthly mean fields of SO_2 and HNO_3 provided by MOZART version 2 [*Horowitz et al.*, 2003] to calculate the rate coefficient for this conversion:

$$k_a = A_o/(A_o + A)\left[3 \times 10^{-9}(SO_2(pptv))\, f(RH) + 5 \times 10^{-9} \cdot (HNO_3(pptv))g(RH)\right], \quad (2)$$

where A_o is the dust aerosol surface area in a diluted plume and A is the simulated dust surface area. The value of A_o is chosen to give a carbonate concentration equivalent to the sum of SO_2 and HNO_3 (monthly average of model outputs) typically found in the Sahara and adjacent tropical Atlantic, as these gases have a large sticking probability to carbonate particles (10–100 times that of other minerals) [*Underwood et al.*, 2001; *Usher et al.*, 2002]. The ratio effectively reduces k_a in intermittent heavy dust concentrations near source regions where SO_2 and HNO_3 are scavenged, and their values are lower than the monthly averages. RH is the relative humidity, $f(RH) = 0$ for RH <50%, $f(RH) = 1$ for RH >60%, and increases linearly from 0 to 1 for RH = 50–60%; $g(RH) = 0$ for RH <25%, $g(RH) = 1$ for RH >35%, and increases linearly for RH = 25–35%. This separate treatment of fresh Saharan dust was discussed previously in *Fan et al.* [2004], where the terms hydrophobic and hydrophillic were used to differentiate between the roles of wet removal.

[12] Fresh Saharan dust particles are converted to acid-coated particles by cloud processing (scavenged by collision and coagulation with cloud droplets, followed by evapora-tion of water) [*Levin et al.*, 1996]. In-cloud scavenging of the unactivated Saharan dust particles by collision occurs by Brownian diffusion, interception, and inertial impaction [*Wurzler et al.*, 2000]. For mineral dust particles, Brownian diffusion and interception are slow processes and are there-fore neglected in this study. Impaction scavenging is calcu-lated on the basis of the cross-sectional area of a spherical particle colliding with a water droplet as follows:

$$Q(r, a) = \pi(r + a)^2 E(r, a)\left(V_d(r) - V_p(a)\right), \quad (3)$$

where r is the radius of the droplet, a is the radius of the particle, $E(r, a)$ is the collection efficiency, $V_d(r)$ is the ter-minal velocity of the droplet, and $V_p(a)$ is the terminal velocity of the particle. We use collection efficiencies given by *Kerkweg et al.* [2003]. The rate coefficient for aerosol transformation to particles removable by water via cloud processing is then given by:

$$k_b(a) = f_{cld} \int_0^\infty Q(r, a)N(r)dr, \quad (4)$$

$$k_b = h(a)f_{cld}, \quad (5)$$

where f_{cld} is the cloud volume fraction diagnosed in the model, and $N(r)$ represents the size distribution of cloud

droplets. We use constant rate coefficients $h(a) = 1 \times 10^{-7}, 2 \times 10^{-5}$, and 3×10^{-5} s^{-1} for $a = 0.1$–1.8, 1.8–3, 3–6 μm, respectively, estimated for typical clean troposphere cloud droplet number concentrations and size distributions.

[13] In this study, we assume that the ambient SO_2 is sufficient to neutralize the $CaCO_3$ in the dust and cause acid coating everywhere in the atmosphere. Strong acids ad-sorbed or produced on mineral dust aerosol first react with carbonates (mainly $CaCO_3$). After all carbonates are neu-tralized in the aerosol, the acidity increases rapidly with additional input of acid molecules. The amount of carbo-nates in each dust particle largely determines how much acid is needed to promote mineral iron dissolution. Single-particle measurements show that dust particles from differ-ent sources are very diverse in mineralogical and chemical compositions and that iron (hydroxy)oxides can exist as individual particles separate from and in aggregate with other minerals (mainly silicates) [*Anderson et al.*, 1996; *Gao and Anderson*, 2001; *Shi et al.*, 2005]. The amount of iron contained in carbonate-rich particles is often low (Z. Shi et al., Influence of chemical weathering and aging of iron oxides on the potential iron solubility of Saharan dust during sim-ulated atmospheric processing, submitted to *Global Bio-geochemical Cycles*, 2010). It is a challenge to model aerosol acidity and iron dissolution for the wide range of internal mixtures of minerals present in the atmosphere. We have conducted two types of simulations in the GCTM: (1) Carbonate content in each dust particle is the same as in the global average soil, and (2) carbonate content is negli-gible in particles with mineral iron. The second assumption causes more rapid aerosol acidification than the first assumption, although the rate of mineral iron dissolution may be chosen to offset this effect in the model. The results presented in this paper are based on the second assumption. However, this does not suggest a preference.

[14] Globally, all non-Saharan source regions are assumed to emit fresh dust particles that can be removed by ice and water clouds. These dust particles are converted to acid-coated particles by cloud processing through droplet nucleation followed by evaporation of water. In the GCTM, the rate coefficient for cloud processing of hygroscopic particles is chosen to convert ~90% of the particles inside the cloud over a 6-h interval:

$$k_c = 1 \times 10^{-4} f_{cld}, \quad (6)$$

for all bin sizes.

[15] The iron in coated dust particles subsequently dis-solves to soluble Fe at a rate k_d determined from a general rate constant on the basis of laboratory measurements [e.g., *Desboeufs et al.*, 1999; *Meskhidze et al.*, 2003; *Mackie et al.*, 2005; *Martin*, 2005; *Cwiertny et al.*, 2008] and adjusted by the length of local sunlight to incorporate the effect of con-version by solar radiation [e.g., *Siffert and Sulzberger*, 1991; *Zhu et al.*, 1997]:

$$k_d = 5 \times 10^{-7}(1 + L(y, t)/12), \quad (7)$$

where $L(y, t)$ is the length of daylight in hours for a given latitude and day of year, producing e-folding values ranging
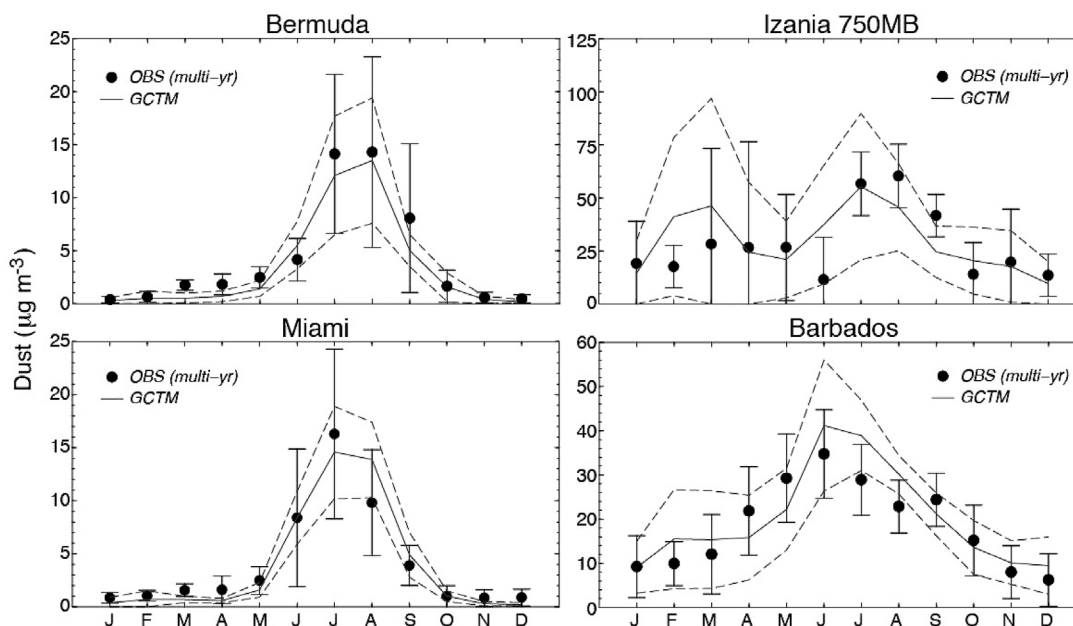
Figure 2. Model and observed multiyear averaged monthly mineral dust surface concentrations (μg m^{-3}) for Barbados (13.2°N, 59.3°W), Miami, Florida, USA (25.5°N, 80.1°W), Bermuda (32.3°N, 64.9°W), and Izania (28.3°N, 16.5°W) located at ~2500 m corresponding to 750 mbar at our model ocean grid box. The bars and dashed line show 1 standard deviation for the observations and the simulation, respectively. Note the different scales of concentration magnitudes.

from 8 to 23 days. The initial solubility of aerosol Fe, which is known to be quite low in both fresh and undissolved, yet coated dust particles [*Zhuang et al.*, 1992b; *Gao et al.*, 2003], is assumed to be 1%. The bioavailable soluble Fe accumulates during transport and is released after ocean deposition [*Buck et al.*, 2006].

[16] Dry deposition of dust aerosols is parameterized according to *Giorgi* [1986]. The dry deposition velocity is expressed in terms of $u*$ and particle size and density. In-cloud wet deposition for highly soluble aerosols is described in *Kasibhatla et al.* [1991]. In-cloud scavenging is assumed to be 100% for dust particles contained in precipitating ice and water drops. The wet deposition parameterization is modified in this study for fresh Saharan dust. Scavenging of fresh Saharan dust is set to zero by water droplet nucleation and is 100% when ice nucleation occurs (ambient temperature below 258°K) in stable clouds or in a convective column. Vertical transport of aerosols in settling raindrops or ice crystals which evaporate below the clouds is calculated as a sink in the cloud layer and a source in the layer below the cloud. The sink is proportional to the rate of settling [*Rogers and Yau*, 1989, p. 125; *Heymsfield and Donner*, 1990; *Westbrook*, 2008] and the cloud fraction, which is diagnosed from the relative humidity [*Slingo*, 1987; *Klein and Hartmann*, 1993; *Campana et al.*, 1994].

[17] It is apparent that the emission, hygroscopic properties, wet and dry removal, chemical conversions, and dissolution to soluble Fe of mineral dust are very complex phenomena that are not entirely well known. Therefore, many assumptions have been made in the model parameterizations of these processes. Even with these simplifications, the model is capable of examining the overall nature

of soluble Fe transport and deposition which, in itself, will be shown to be quite complicated.

3. Model Evaluation

[18] The GFDL GCTM simulation was run over the period from 1994 to 2006 with appropriate data saved every 6 h, allowing comparisons on timescales ranging from annually to daily, with observed mineral dust concentrations and deposition, dust iron solubility in aerosols and precipitation, and bioavailable soluble iron flux to the ocean. Multiyear monthly model means are computed over 13 years of integration, while available measurements are from varying time periods. Monthly averages for individual years and episodic time series are compared over the actual time period and year.

3.1. Mineral Dust Concentrations

[19] Over the North Atlantic Ocean, surface dust concentrations exhibit a strong seasonality. Figure 2 compares multiyear monthly averaged in situ observations with model values at four geographically arranged sites at varying distances from the Sahara dust source region: Bermuda in the western Atlantic; Izania in the eastern Atlantic; Miami, Florida, USA, at the western edge of the Atlantic; and Barbados near the eastern Caribbean Sea. (The dashed lines and bars show 1 sd for the model and observations, respectively.) The GCTM adequately simulates the summer maximum and the variability at Barbados, Miami, and Bermuda, as well as the decrease in concentration values with transport distance from the Sahara.

[20] In contrast, Izania exhibits a concentration maximum in summer and spring, large values, and high variability.
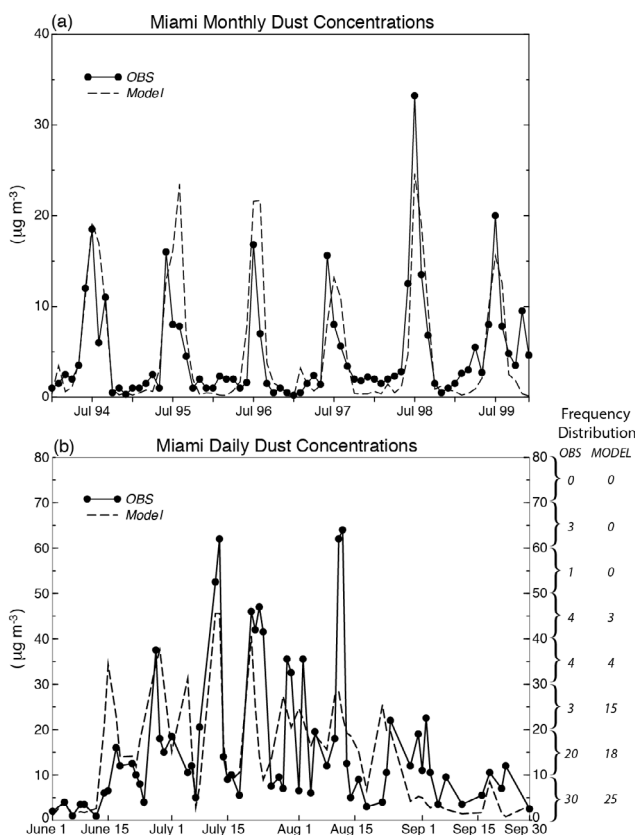
Figure 3. (a) Model and observed monthly average time series of mineral dust concentrations (μg m^{-3}) from January 1994 to December 1999 at Miami. (b) Model and observed daily time series of mineral dust concentrations for 65 observation dates from 1 June 1999 to 30 September 1999 at Miami. The observed and modeled frequency distributions for bins of 10 μg m^{-3} are presented to the right of Figure 3b.

This arises as a result of its close proximity to the Saharan dust sources and its more northerly location. Izania is far enough north and east that its winter and spring meteorology is controlled by variations in the jet stream westerlies, allowing intermittent export of dust northwestward into the region [*Moulin et al.*, 1997]. The model simulates the spring and summer peaks and the large spring variability; however, the spring maximum is earlier and somewhat larger and the June minimum is not captured.

[21] While the GCTM simulates the observed multiyear large standard deviations in the summer western Atlantic reasonably well, it is more problematic to model the actual maximums and minimums on shorter time scales. Figure 3a

compares model surface dust concentrations at Miami with observed January 1994 through December 1999 monthly mean values [*Prospero and Landing*, 2007], and Figure 3b compares them with Miami daily mean values (1 June through 30 September 1999) [*Lenes et al.*, 2001]. The GCTM captures the general timing and magnitude of the summer maximum for individual years, although some years can be ~30% higher or lower, and August is overpredicted (also apparent in Figure 2). When daily comparisons are examined, we see that the monthly means are actually composed of numerous short-term dust events. The model produces these episodes and generally agrees with the observed timing, although there can be substantial errors in the magnitude. The frequency distribution to the right of Figure 3b, based on 65 observation days, reveals that both observations and the model have a similar distribution of binned values with numerous low-magnitude concentrations (<20 μg m^{-3}) dropping off sharply to relatively few events having concentrations >30 μg m^{-3}. While there are four observed events greater than 50 μg m^{-3}, the model produces none. However, an examination of the simulation during nonobservation days of the 3-month period showed 2 days of values >50 μg m^{-3}, indicating that the model is capable of generating large dust episodes.

3.2. Mineral Dust Deposition

[22] Previous modeling studies have shown that the North Atlantic Ocean receives the largest fraction of the world ocean mineral dust deposition, estimated at 43% in the North Atlantic Ocean, 25% in the Indian Ocean, 15% in the North Pacific Ocean, and 17% other [*Ginoux et al.*, 2001; *Tegen et al.*, 2002; *Mahowald et al.*, 2003; *Jickells et al.*, 2005]. Table 2 shows that predicted annual deposition into the North Atlantic Ocean ranges from 178 to 259 Tg. Models have inherent parameterization uncertainties but can provide a detailed global analysis of dust flux, while in situ measurements, utilizing surface concentrations and assumed scavenging ratios, can estimate local totals [*Duce and Tindale*, 1991; *Prospero*, 1996]. Validation of the model, however, is difficult. The only available observed ocean flux data are sparse annual estimates using deep ocean sediment traps that have their own intrinsic problems as a result of ocean surface transport and slow effective sinking rates [e.g., *Lam et al.*, 2006] as well as mixing from below. Dust fluxes also can be affected by the column biological activity above the traps [*Bory and Newton*, 2000], and flux estimations are difficult to make for small samples found distant from dust source regions. Figures 4a and 4b compare the spatial distribution of the model 13-year average annual mineral dust deposition with compiled sediment trap data [*Kohfeld and Harrison*, 2001]. Overall, the model and data are qualitatively similar.

Table 2. Deposition Into the North Atlantic Ocean[a]

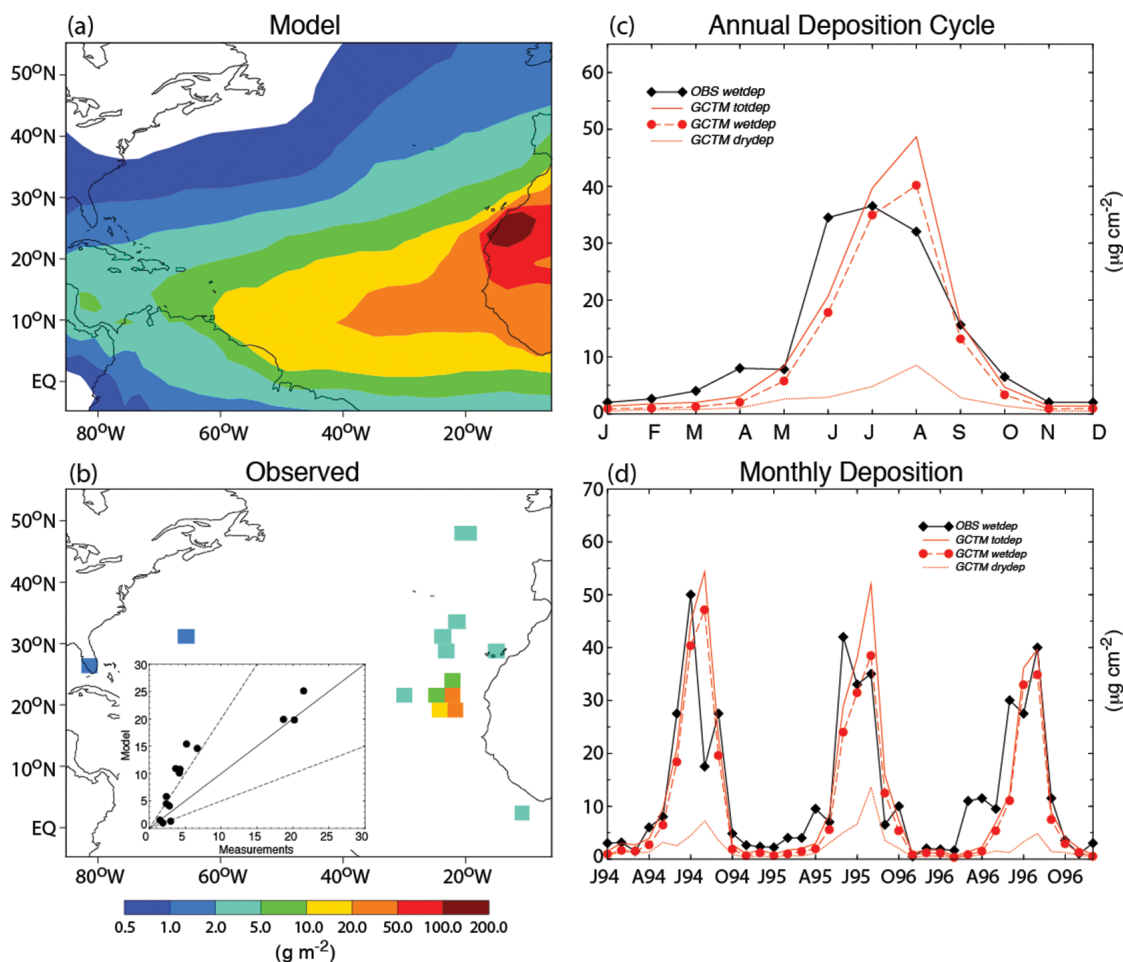|	Duce and Tindale [1991]	Prospero [1996]	Ginoux et al. [2001]	Zender et al. [2003]	Tegen et al. [2002]	Luo et al. [2003]	This Study
Dust	220.0	220.0	184.0	178.0	259.0	230.0	245.0
Total Fe	7.7	7.7	6.4	6.2	9.1	8.1	8.6
5% soluble Fe	0.4	0.4	0.3	0.2	0.5	0.4	0.4
Variable soluble Fe							0.9

[a]Units are in Tg yr^{-1}.

Figure 4. (a) Model annual mineral dust deposition (g m^{-2}). (b) Observational estimates (g m^{-2}) from DIRTMAP [*Kohfeld and Harrison*, 2001]. Inset shows model values versus observational estimates (solid line indicates a 1:1 relation; dashed line indicates a 2:1 relation) at the presented measurement sites. (c) Annual cycle of observed monthly dust wet deposition and model wet, dry, and total deposition (μg cm^{-2}) for the state of Florida averaged over 3 years (1994 to 1996). (d) Florida monthly time series of observed dust wet deposition and model wet, dry, and total deposition (μg cm^{-2}) from January 1994 to December 1996. For Figures 4c and 4d, observed data are averages of nine Florida stations [*Prospero et al.*, 2010] and simulated data are averages of Florida grid boxes.

The simulation depicts the weak east-west gradient and tighter north-south gradients seen in the measurements, although the extremely sharp gradient off the west coast of Africa is not apparent. In general, as shown in the Figure 4b inset, model values are somewhat higher than the observations, but within or near a factor of 2.

[23] Mineral dust flux measurements on shorter temporal scales are uncommon. However, an extensive data set exists across the state of Florida for the years 1994 through 1996, when monthly wet deposition was compiled at nine individual sites [*Prospero et al.*, 2010]. Figures 4c and 4d show the annual cycle of monthly wet deposition averaged over the 3 years and the actual monthly time series over the 36-month period, respectively, where the nine data stations as well as the model's three Florida peninsular grid boxes have been correspondingly averaged. The winter-spring simulated deposition values are underestimated, and the

maximum mean deposition tends to occur later in summer; however, the maximum magnitude of the wet deposition is within 15% of the observed value. While the 3-year average seasonal cycle is depicted reasonably well, the 36-month time series shows that individual months can differ significantly. The simulated wet deposition for August 1994 is greatly overestimated, although the summer months of 1995 and 1996 are more realistic. The model also indicates that the 3-year average wet to total deposition ratio is quite large at this location during the August seasonal maximum (~82%), although 1995 produced a lower ratio of ~73%, indicating some variability in the role of dry deposition.

3.3. Iron Solubility

[24] Table 1 presents a summary of available measurements of the soluble Fe fraction in aerosols and precipitation compared with the model simulation. Where possible, we
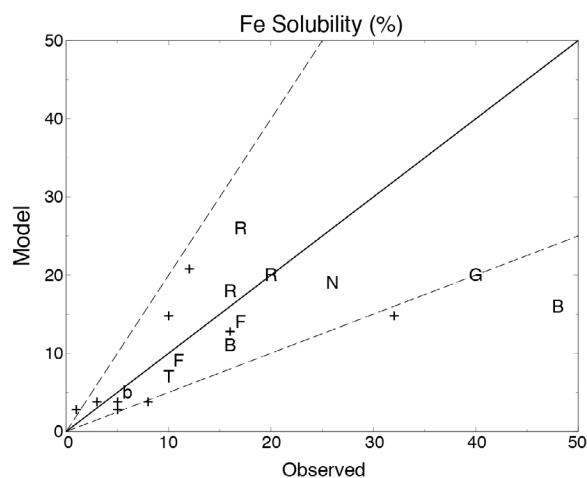
Figure 5. Model versus observed Fe solubility (expressed as a percentage) from Table 1 for sites in the general North Atlantic basin and sites close to the Sahara desert (solid line indicates a 1:1 relation; dashed line indicates a 2:1 relation). The sites are Bermuda (indicated by B), Barbados (indicated by b), France (indicated by F), Greenland (indicated by G), North Carolina (indicated by N), Rhode Island (indicated by R), Turkey (indicated by T), and various cruise locations (indicated by crosses).

use the same month and year and grid boxes representing the observation location or cruise tracks. For older values prior to the start of our simulation, we used our 13-year average for the appropriate time period. There is a wide range of Fe solubility ranging from 1 to 8% off the west coast of Africa, to 40% in Greenland ice core samples, to 56% in the Hawaiian Islands. In a broad sense, there is an increase in solubility with seasonal transport distance from dust source regions as dust concentrations decrease due to wet and dry removal as well as diffusion. The soluble Fe fraction is a function of transport time and the path taken. This is indicated in the North Atlantic Ocean, where dust exiting from West Africa is characteristically transported by the subtropical Azores high-pressure system west to the Caribbean and then northward in the western Atlantic. As depicted in Figure 5, low values are found in the Saharan subtropical dust plume (Barbados and ship cruises), while higher values are seen farther west and north in Bermuda, North Carolina, and Rhode Island. Dust can also be transported northward from the Sahara to Europe, where, in addition to transport time, interactions with pollution can play a role. Overall, the model simulates the soluble Fe fraction qualitatively well, and model values are found within a factor of 2 of the measurements with a few outliers.

[25] The Barbados observation and the September and November data provided by the cruises of *Baker et al.* [2006a, 2006b] depict a unique north-south transect where relatively high solubility north of 25°N, from roughly France to the Canary Islands at ~15°W, decreases within the high dust concentrations off the coast of Africa (21°N-6°N, 18°W) and then increases again in the tropical South Atlantic Ocean. This observed north-south Fe solubility variation is captured by the model, although the simulated South Atlantic Ocean values are larger.

3.4. Indirect Assessment of Soluble Iron Deposition

[26] While sparse measurements of dust Fe solubility in aerosols and precipitation are available, at present no direct measurements of SFeD exist. There have been studies, also sparse in space and time, where dry and wet Fe flux has been inferred [e.g., *Sarthou et al.*, 2003; *Sedwick et al.*, 2005; *De Jong et al.*, 2007]. While these observations present an indirect estimate of the overall iron fluxes, they are not a direct measurement and they do not provide detailed information on event-based deposition of bio-available iron resulting from episodic Saharan dust storms and subsequent transport. Models, on the other hand, produce detailed SFeD data on various time and space scales, but have no direct observations to evaluate results.

[27] One can determine if the model-generated SFeD is reasonable by utilizing data from various cruises where significant changes in mixed layer dFe were measured while traversing the same region over relatively short time periods. An increase in dFe can occur from atmospheric SFeD and/or ocean upwelling and entrainment of Fe from lower depths and can be affected by scavenging or biological uptake of dFe within the euphotic zone. However, by selecting a time and location where SFeD should be a dominant process (e.g., a dust deposition event in a nutrient poor, thermally stratified surface mixed layer, where entrainment from below and biological processes are negligible), the simulated accumulation of SFeD ought to be in the range of the observed change in dFe.

[28] We present the model accumulated SFeD for two scenarios: variable solubility using the *Fan et al.* [2006] parameterization and constant 2% simulated at the location and time period for two distinct measurement campaigns: cruise 1 off the coast of Spain and Portugal (~43°N, 20°W) close to Saharan dust source regions during March 1998 [*De Jong et al.*, 2007] and cruise 2 in the Sargasso Sea (~31°N, 65°W) from 24 July to 6 August 2003 [*Sedwick et al.*, 2005] (Figures 6a and 6b, respectively).

[29] Early in cruise 1, 6–8 March, large sea surface dFe values were measured averaging ~1.9 nM within subtropical gyre waters as inferred by salinity and temperature measurements. These samples were taken just after one of the largest Saharan dust outbreaks of that decade experienced in the Canary Islands from 11 February through 5 March [*Pérez-Marrero et al.*, 2002; *Torres-Padrón et al.*, 2002], with deposition impacts northward into the Atlantic. The model mineral dust concentrations compare well with the observed 800 mbar (2 km) episodes (Figure 6c), adequately capturing the large events of early and late February.

[30] On the return cruise transect (22–23 March), when atmospheric dust input had returned to background values (no observed dust outbreaks; note that there is only minor simulated SFeD after 6 March), dFe had decreased to a more typical relatively low value of ~0.6 nM. This dFe change of 1.3 nM within a reported mixed layer depth of 50 m would require a soluble Fe loading of 65 μmol m^{-2} prior to 6 March. The simulated 71.0 μmol m^{-2} (1.4 nM) SFeD accumulation based on variable solubility is near this value
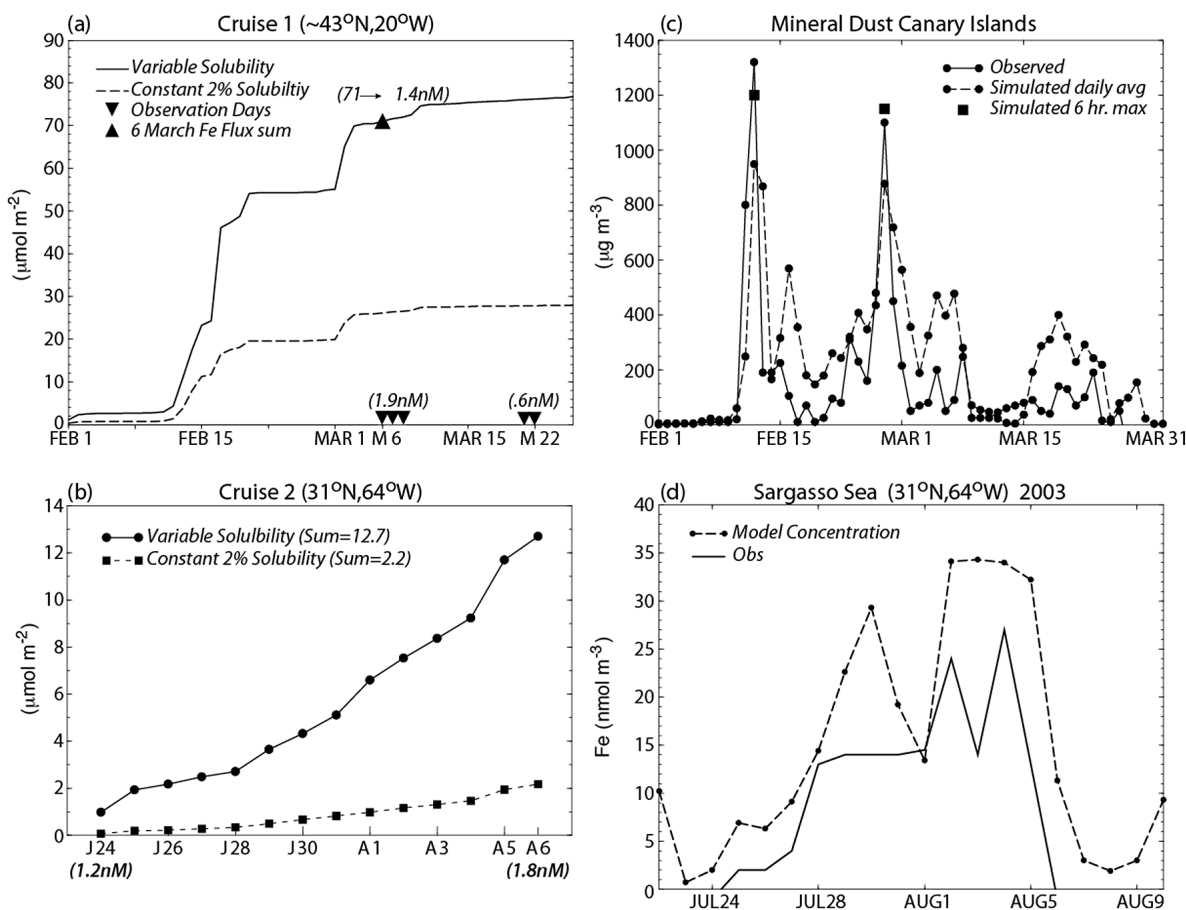
Figure 6. Simulated accumulation of daily total (wet + dry) soluble Fe deposition (SFeD) (μmol m^{-2}) for two observational cruises (a) off the coast of Spain (43°N, 20°W) from February through March 1998, with the downward triangles at the bottom of the figure representing the transit dates of the dissolved Fe measurements and their values in parentheses and the upward triangle indicating the simulated soluble Fe flux sum (71 μmol m^{-2}) on 6 March. (b) The Sargasso Sea (31°N, 64°W) from 24 July through 6 August 2003. The observed dissolved Fe values are presented under appropriate dates. (c) Model and observed daily time series of mineral dust concentrations (μg m^{-3}) at 800 mbar in the Canary Islands from February through March 1998. The large black squares are the simulated 6-h maximums for a particular day. (d) Model comparison with observed daily time series of Fe concentrations (nmol m^{-3}) in the Sargasso Sea from 24 July through 6 August 2003.

(upward triangle in Figure 6a), while constant 2% produces only 26.1 μmol m^{-2}.

[31] In contrast, cruise 2 took place far from the Saharan desert source region, where strong summer mixed layer stratification (20 m) was observed in thermally stratified, nutrient-poor waters south of Bermuda, suggesting negligible redistribution of iron from below. During the 13-day period from 24 July to 6 August, satellite images revealed that the region was affected by a Saharan dust plume. During this time, cruise 2 observed a high loading of total aerosol Fe and measured an increase in mixed layer dFe of 0.6 nM. The timing of the event was successfully simulated by the GCTM (Figure 6d). The model produced two pulses of mineral dust. The first occurred during an absence of cruise 2 measurements (29 July to 1 August is an extrapolation of 28 July). Over the same time span, the simulated

cumulative SFeD based on variable solubility generated a value of 12.7 μmol m^{-2}. In comparison, constant 2% solubility produced a value of only 2.2 μmol m^{-2} (Figure 6b). Within a mixed layer depth of 20 m, these values would produce increases of 0.64 nM and 0.11 nM, respectively. The GCTM parameterization, where the soluble iron fraction increases with transport time, produces a plausible SFeD, whereas holding solubility at an assumed constant does not.

[32] This discrepancy could be an important factor in the iron cycling simulated in biogeochemistry models. *Aumont et al.* [2008] used an ocean biogeochemistry model to examine the variability of dFe over various timescales. Their model variability over timescales similar to *Sedwick et al.* [2005] (13 days) within the northern subtropical gyre of the Atlantic Ocean produced maximum variations in dFe of only 0.2 nM compared to the observed local value of
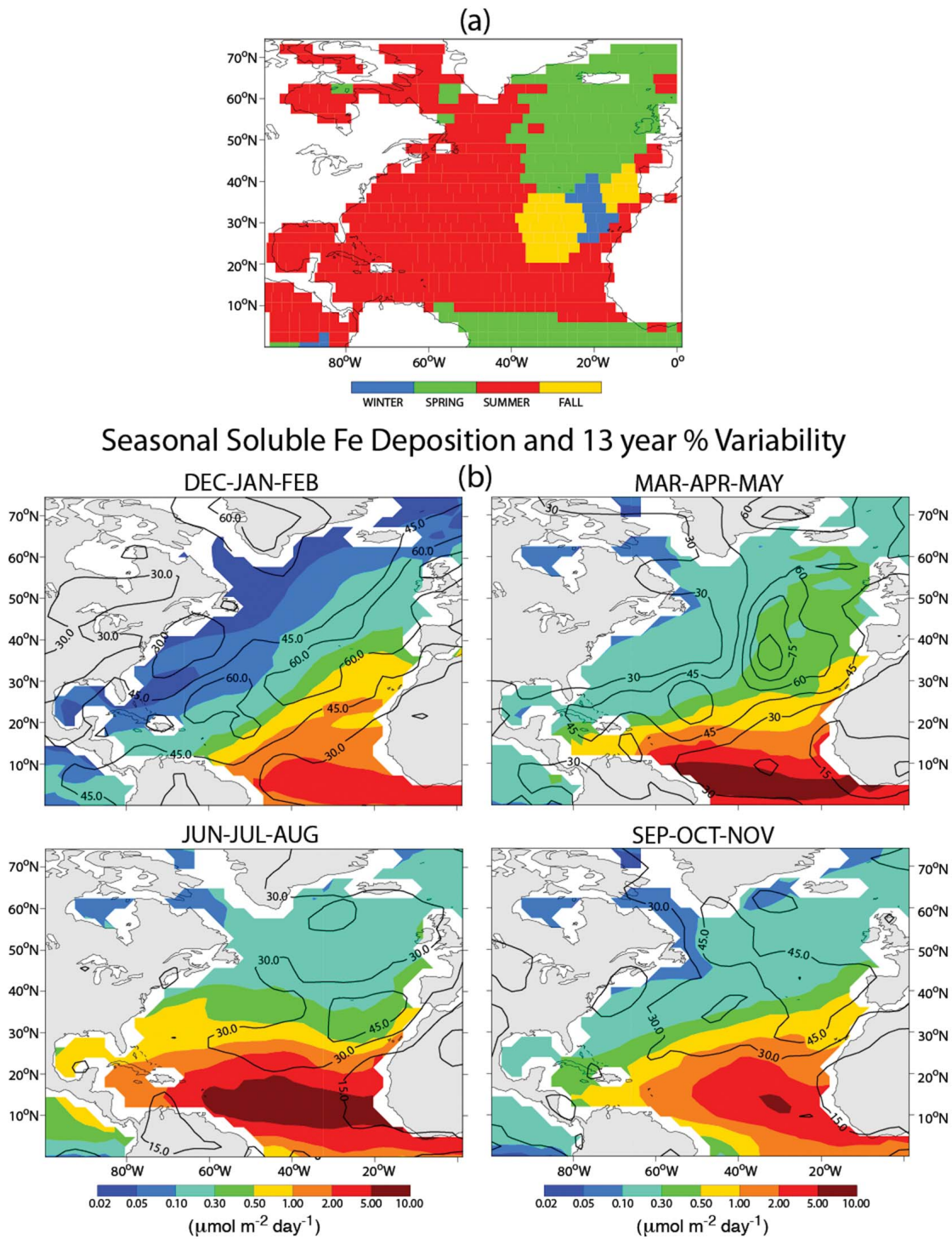
Figure 7. (a) Season of model maximum SFeD on the basis of 13 years of integration (1994 to 2006). (b) Simulated seasonal average SFeD magnitude (μmol m^{-2} d^{-1}) and year-to-year standard deviations (expressed as percentages) as indicated by color shading and contour lines, respectively.

0.6 nM, discussed above. However, they acknowledged that by assuming only a constant 1% Fe solubility, "even strong dust events have only a small imprint on surface iron concentrations."

[33] A more detailed model analysis of cruise 2 dust concentrations, wet and dry SFeD, percentage Fe solubility, and transport meteorology is presented in section 4.3, and an examination of the relative magnitude of short-term bursts
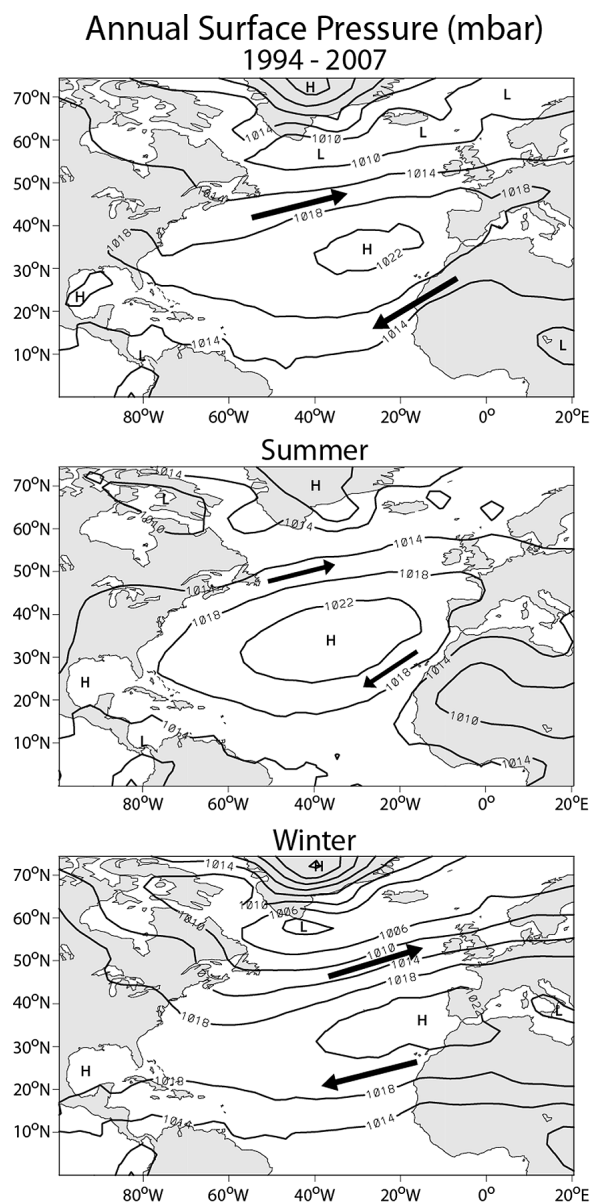
Annual Surface Pressure (mbar)
1994 - 2007

Figure 8. Annual, summer, and winter average surface pressure (mbar) in the North Atlantic basin. The arrows depict the general directional circulation.

of SFeD (days) as compared to monthly mean rates is presented in section 5.

4. Transport Meteorology: Mineral Dust and SFeD Variability

[34] In this section, we investigate the meteorological aspects of soluble iron transport and deposition. The wind and surface pressure fields described here are based on NCEP reanalysis data [*Kalnay*, 1996].

4.1. Seasonal

[35] Although it is well known that long-term deposition of mineral dust is actually an accumulation of numerous shorter-term events [e.g., *Prospero*, 1999; *Prospero and*

Lamb, 2003], it is nevertheless useful to examine the large-scale transport meteorology and deposition distribution. Figure 7a shows the season of maximum simulated SFeD, and Figure 7b shows its seasonal magnitude and temporal relative standard deviation over the 13-year period from 1994 to 2006.

[36] The bulk of the North Atlantic Ocean receives its maximum SFeD during summer, while the greatest deposition in the northeast Atlantic is found during March through May, coincident with the observed spring bloom (Figure 7a). Farther south, off the coast of northwest Africa, is a region without any clear seasonal dominance. The largest seasonal flux (>5 μmol m^{-2} d^{-1}; >450 μmol m^{-2} season^{-1}) occurs in the subtropics during summer (Figure 7b), when dust is transported westward off Africa by steady trade winds as seen by the relatively low (<30%) variability. During winter and spring, large year-to-year variability (>60%) is seen in the central Atlantic from north of the Caribbean to the west of Europe. Regionally, a near absence of SFeD during some years and large episodes during other years produces very high variability (>75%) as depicted in the central north Atlantic.

[37] The principal atmospheric circulation system in the North Atlantic Ocean is the subtropical Azores high pressure (subsequently referred to as the "Azores High"), presented in Figure 8. Its annual average circulation encompasses the entire region from the midlatitudes to the tropics transporting pollution from Europe [*Church et al.*, 1990; *Kim and Church*, 2002] and dust from the Sahara anticyclonically to the Atlantic. During summer, the entire North Atlantic is under the influence of the Azores High, while in winter the strong pressure gradient south of Iceland allows prevailing west-east winds to penetrate farther south. This interaction of midlatitude westerlies with the Azores High, known as the NAO [*Hurrell*, 1995], can dramatically alter the regional transport.

[38] During winters with a positive NAO (NAO+), the Azores High strengthens and the Icelandic low pressure deepens, while a negative NAO (NAO−) indicates a period of much weaker north-south pressure gradient. This is depicted in Figure 9a, which shows a strong positive correlation between the NAO index and the Azores High and a strong negative correlation with the Icelandic low pressure. Figures 9b and 9c are examples of winter surface pressure for a strong NAO+ year (2000, +2.80) and a strong NAO− the following year (2001, −1.85). During the NAO+, the Azores High is stronger than average, with a greater eastern extent producing increased subsidence and drier regional conditions as well as a stronger pressure gradient to the south. Also, the midlatitude storm track is shifted farther north toward northern Europe. In contrast, the NAO− seasonal circulation presents a significantly weaker pressure gradient field, which is a result of a more southern storm track over the central Atlantic, where synoptic scale low-pressure systems modify the seasonal Azores High.

[39] These large changes in the meteorological pattern significantly affect the regional transport circulation and precipitation, which in turn influence mineral dust mobilization, atmospheric loading, and deposition. This has been demonstrated by both observations and model simulation. With the advent of available satellite aerosol optical depth data, *Moulin et al.* [1997] were the first to suggest a relationship between the NAO and the pattern and strength of
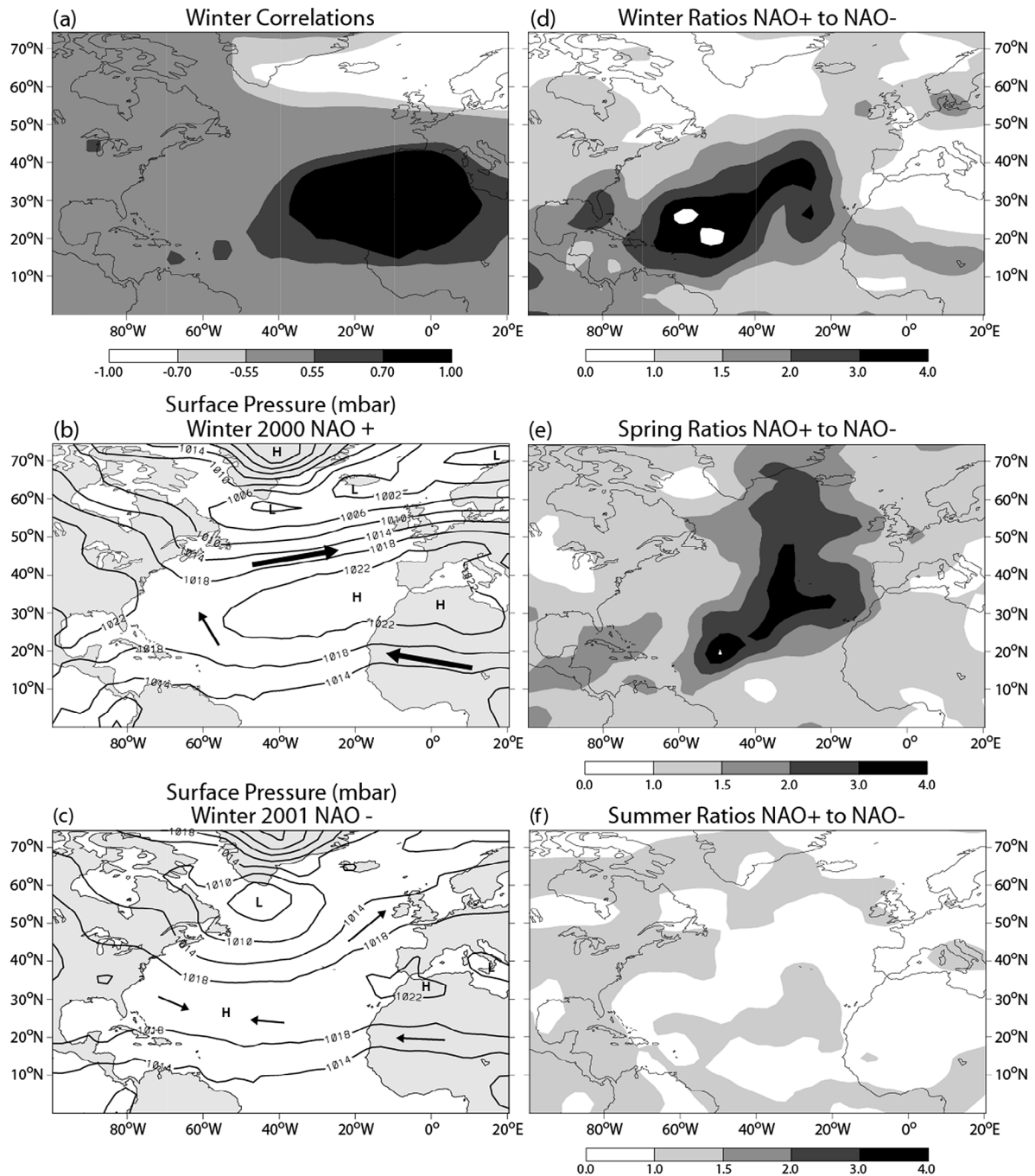
Figure 9. (a) Map of the correlation coefficient between winter surface pressure and the North Atlantic Oscillation (NAO) over 13 years (±0.7, 99% significant). (b) Winter (December-January-February) surface pressure during a strong NAO positive (NAO+) year (2000). The arrows depict the general strength (thicker implies stronger) and direction of circulation. (c) Same as in Figure 9b except for a strong NAO negative (NAO−) year (2001). (d) Winter SFeD ratio of the average of strongly NAO+ years to the average of strongly NAO−years. (e) Spring SFeD ratio. (f) Summer SFeD ratio.

Saharan dust transport. *Chiapello and Moulin* [2002] used a long-term data set (1979 to 1997) that showed large year-to-year variability of Saharan winter dust transport and provided evidence of a NAO influence producing enhanced column dust values off the northwest coast of Africa during a NAO+ year. Utilizing a long-term model simulation,

Ginoux et al. [2004] demonstrated a positive correlation between the winter NAO and dust concentrations over much of the North Atlantic and the Sahara. This is attributed to an increase in dust emissions over the Bodele-Lake Chad region resulting from stronger surface winds over North Africa during NAO+ years. The work of *Riemer et al.*
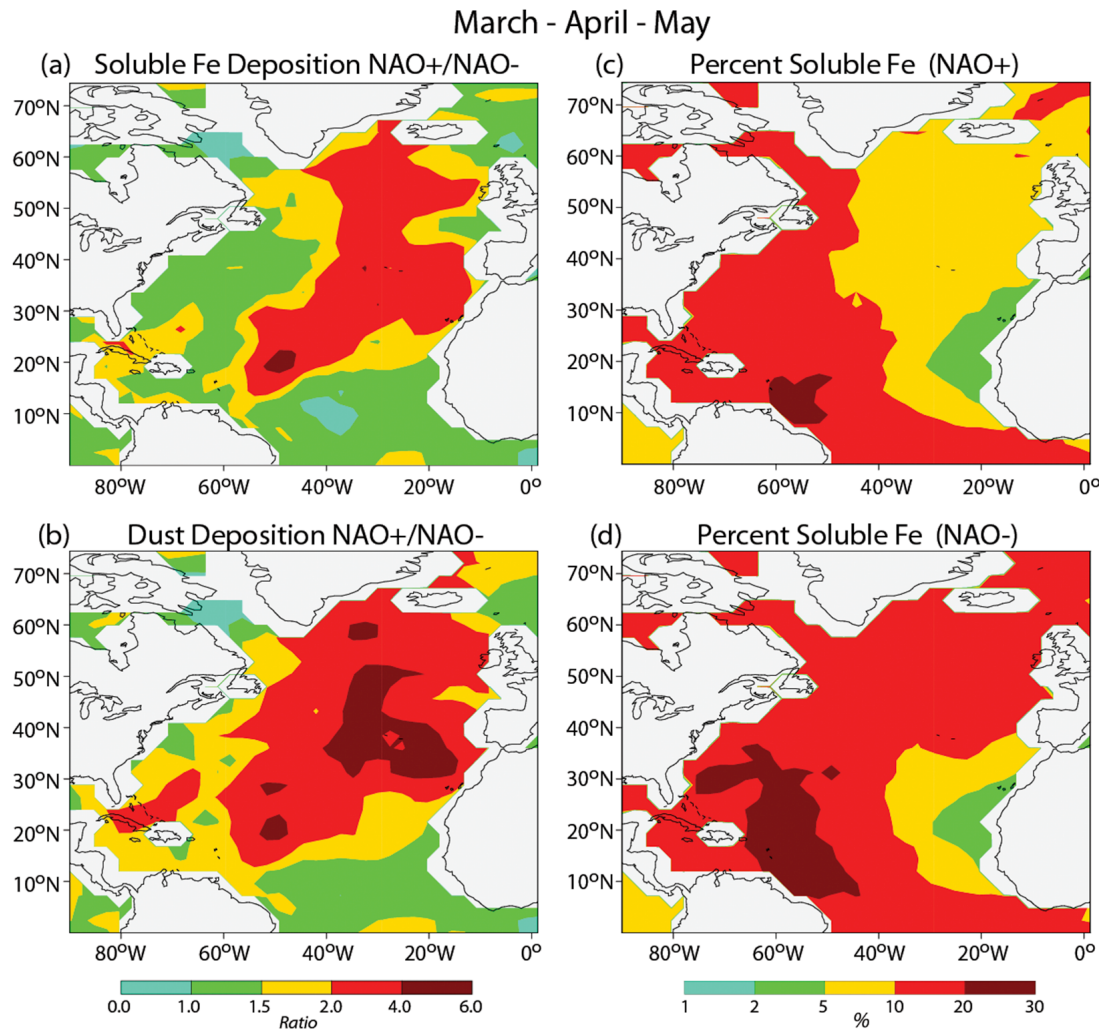
Figure 10. Spring ratio of the average of strongly NAO+ years to the average of strongly NAO− years for (a) SFeD and (b) mineral dust deposition. Soluble Fe fraction (%) for (c) NAO+ years and (d) NAO− years.

[2006] suggested that the winter position of the Azores High rather than the NAO pressure differential was the more important factor in Saharan dust transport. The export of African dust was shown to be larger during years when the Azores High was located north of its climatic mean position.

[40] The variations in the NAO can also have a profound influence on the SFeD seasonal variability. Over the years 1994 through 2006, there were four strongly positive NAO years (1994, 1995, 1999, and 2000; values >1.) and three strongly negative years (1996, 2001, and 2006; values <−1.). Figures 9d–9f present the SFeD ratios of the average of the strong NAO+ winters to the average of the strong NAO− winters for three seasons. The enhanced mineral dust transport during NAO+ years, as indicated by previous studies, greatly augments SFeD. The SFeD ratio is larger than a factor of 2.0 over a large area of the central Atlantic during winter and extends to the North Atlantic during spring. In general, the axis of maximum ratios coincides with the region of maximum temporal standard deviation (see Figure 7b). During summer, the weakened midlatitude westerlies have retreated north and no longer interact with

the Azores high. Transport is governed essentially by minor variations in the strength and positions of the Azores high itself.

[41] While it is apparent that SFeD increases are linked to mineral dust transport during NAO+ years, it is important to examine the role, if any, played by variations in Fe solubility. Figures 10a and 10b depict the spring ratio of NAO+ years to NAO− years for SFeD and mineral dust deposition, respectively. The distributions of the two ratio fields are quite similar; however, the magnitude of the mineral dust deposition ratio is larger. This implies transport domination with the magnitude of SFeD being modified by variations in Fe solubility. During high SFeD NAO+ years associated with rapid transport from the Sahara to the central Atlantic (less dissolution time), relatively low Fe solubility is found (Figure 10c), while higher Fe solubility (Figure 10d) and low SFeD during NAO− years are related to low concentrations in background aged dust. This effectively dampens the SFeD magnitude during NAO+ years and enhances it during NAO− years, thereby decreasing its ratio in comparison with mineral dust.
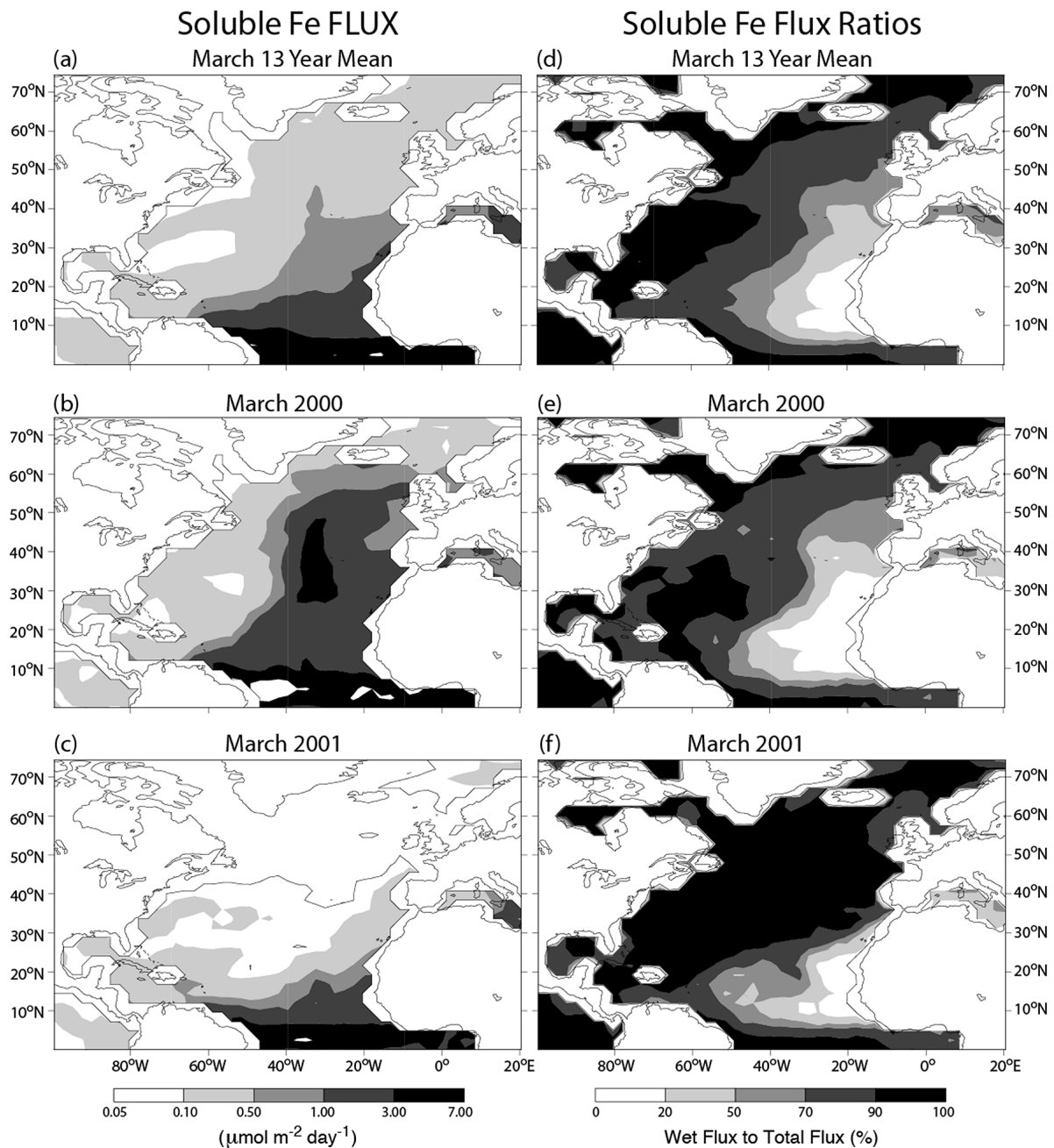
Figure 11. March soluble Fe ocean total deposition (μmol m^{-2} d^{-1}) for (a) 1994 to 2006 average, (b) March 2000, and (c) March 2001. March SFeD ratio of wet deposition to total deposition (%) for (d) 1994 to 2006 average, (e) March 2000, and (f) March 2001.

4.2. Monthly to Synoptic Scale: Winter-Spring Regime

[42] One would expect larger year-to-year swings in the SFeD when examining individual dust outbreaks where variability in meteorological transport patterns can alter regional deposition. Figures 11a–11c describe the March mean SFeD for the 1994–2006 average, 2000, and 2001, respectively. It is apparent that the long-term 13-year March mean contains a great range of SFeD. During late February and March 2000 (NAO+), strong episodic outbreaks of Saharan dust into the Atlantic off the northwest coast of Africa were observed [*Cana*, 2002; *Ryall et al.*, 2002],

which generated very large simulated monthly SFeD over the central and northeast Atlantic (>1 μmol m^{-2} d^{-1} with maximum values >3). In comparison, the following year (2001, NAO−) produced mid-Atlantic values of only ~0.05 μmol m^2 d^{-1}, 60 times less. This was a result of the bulk dust transport shifting southward into the tropical Atlantic off the southwest coast of North Africa.

[43] On the basis of evidence provided by both observations and model simulations of wet and dry mineral dust deposition, it is generally accepted that wet removal of mineral dust dominates dry removal over remote ocean regions,
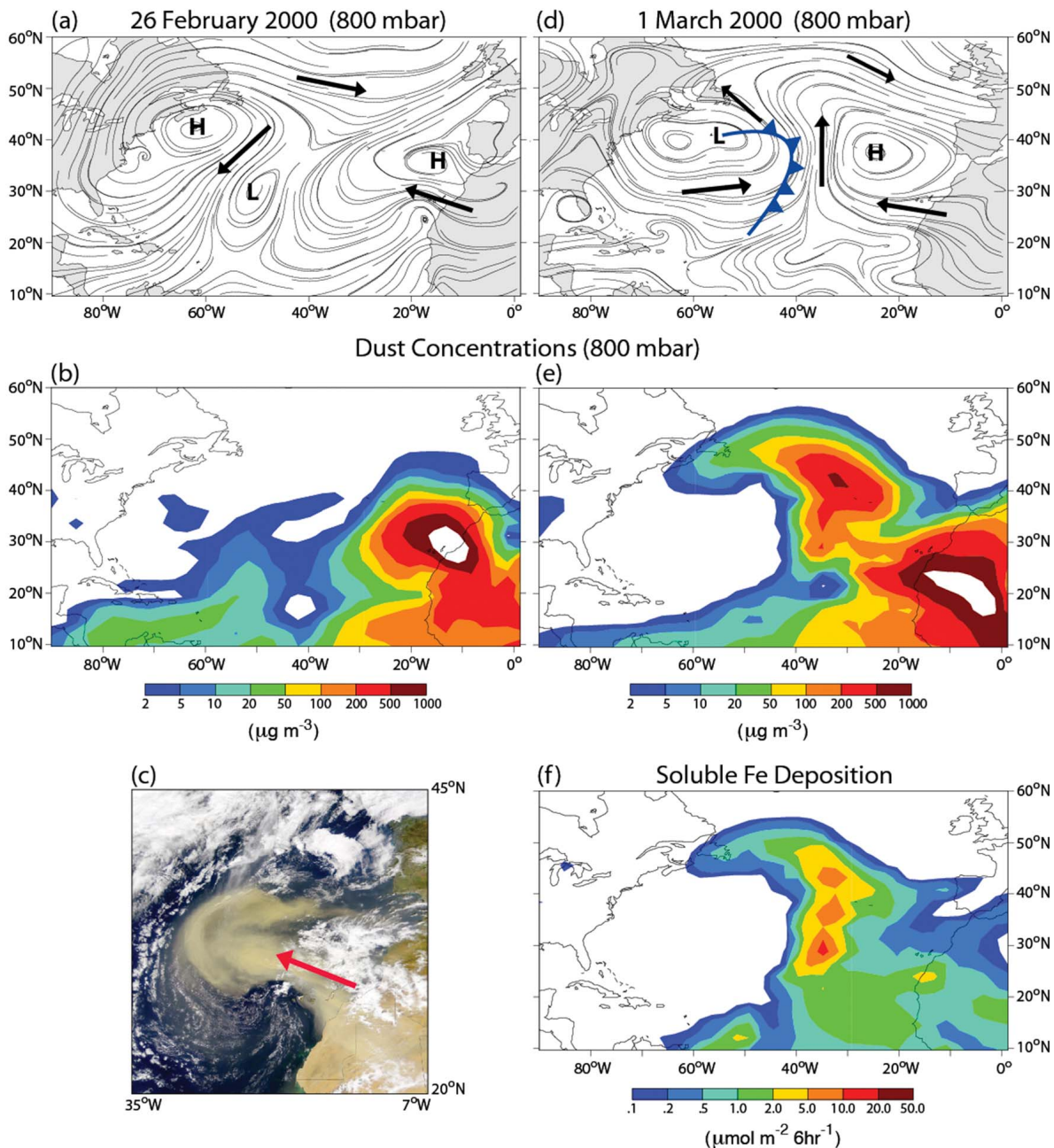
Figure 12. Synoptic scale transport and deposition event of 26 February to 1 March 2000. (a) 800 mbar (~2 km) streamlines (arrows and lines depict the direction of flow; "H" and "L" represent high and low pressure centers, respectively) on 26 February corresponding to (b) mineral dust concentration (μg m^{-3}) at 800 mbar and (c) satellite observed dust exiting northwest Africa (SeaWiFS Project, GSFC, and NASA). (d) 800 mbar streamlines (arrows and lines depict the direction of flow; thick blue line with triangles represents the cold front) on 1 March corresponding to (e) mineral dust concentration (μg m^{-3}) at 800 mbar and (f) SFeD (μmol m^{-2} 6 hr^{-1}).

while dry removal is more important near dust source regions [e.g., *Uematsu et al.*, 1985; *Duce and Tindale*, 1991; *Gao et al.*, 2003; *Hand et al.*, 2004; *Fan et al.*, 2006]. This can be seen in the 13-year March mean ratio of simulated wet SFeD to total SFeD (Figure 11d). Off the west coast of Africa near the Saharan source region, significant mineral dust transport and low precipitation produce large dry deposition dominated SFeD. In contrast, wet removal controls

deposition over the more distant west and central Atlantic, but is coincident with the weaker SFeD depicted in Figure 11a. Mineral dust in the remote Atlantic is a consequence of irregular long-range transport, sedimentation removal of larger particles, and continual wet and dry deposition. The result is a well-mixed, low-concentration dust background where intermittent column removal by precipitation is greater than surface dry deposition; however, the overall SFeD is

generally small. This effect is amplified during a year with negligible transport to the remote ocean, where the Fe flux is almost entirely from wet deposition but SFeD is insignificant (Figures 11c and 11f).

[44] During years with large SFeD dominated by regional wet removal (Figures 11b and 11e), monthly spatial structure is controlled by synoptic scale weather systems and dust transport episodes. The average March 2000 SFeD is in actuality a product of several short-term deposition events that took place during the month, the largest of which occurred on 1 March. The complexity of the episode can be seen in Figure 12. On 26 February, the Azores High is located off the northwest coast of Africa, producing a strong east-west transport of dust from the Sahara over the Canary Islands into the Atlantic as simulated by the GCTM and depicted by satellite (Figures 12a–12c). A weak storm system situated over the south-central Atlantic in a near dust-free region propagates north and strengthens, generating a strong cold front and associated rainfall in the central Atlantic by 1 March (Figure 12d). During this time (Figures 12e and 12f), dust has been transported anticyclonically around the Azores High into the precipitation area east of the cold front, producing significant SFeD (>2 μmol m^{-2} 6 h^{-1} over a substantial area; note the sharp decrease in both dust and SFeD to the west of the cold front). This type of transport pattern is very similar to the March 1998 dust outbreak that was associated with the high dFe levels observed during cruise 1 and discussed in section 3.4.

4.3.   Summer Regime Event Study
4.3.1.   Mineral Dust Transport Evolution

[45] While intermittent springtime Atlantic SFeD events evolve from timely interactions of midlatitude weather systems with Saharan dust outbreaks, one would anticipate that during the relatively steady summer trade wind flow around the southern base of the Azores High, dust transport episodes crossing the Atlantic would be considerably less complex. It is well known that strong desert heating during summer forms a deep, mixed Saharan dust layer that can extend up to 500 mbar. The mineral dust can then be transported westward across the Atlantic, usually in association with easterly waves, while embedded within the Saharan air layer, a dry warm stable region above the cool, moist marine boundary layer of the Atlantic ocean [e.g., *Burpee*, 1972; *Prospero and Carlson*, 1972; *Carlson and Prospero*, 1972; *Ott et al.*, 1991; *Karyampudi et al.*, 1999; *Jones et al.*, 2003; *Wong et al.*, 2006]. As seen in numerous satellite depictions, these dust pulses appear to simply move slowly from east to west across the Atlantic [e.g., *Huang et al.*, 2010] and eventually mix down to the surface or are removed by wet and dry deposition. However, when an observed subtropical dust event is analyzed in detail, the transport processes are found to be quite intricate.

[46] The analysis benefit of dust transport models is that simulated data are available at all grid boxes at all selected times. If the magnitude and timing of a particular observed event is adequately simulated, the transport path and origin can be examined in detail. In this context, we reexamine the 24 July to 6 August 2003 high dust concentration episode observed in the Sargasso Sea during cruise 2 [*Sedwick et al.* [2005], referred to in section 3.4 and Figures 6b and 6d of

this paper) and specifically analyze the onset of the 2 August maximum.

[47] To obtain a general feel for the event's time evolution, we can first assume that the dust was horizontally transported within the Saharan air layer and examine the sequential 850 mbar concentration fields (Figures 13a–13e). On 25 July, dust was just exiting the west coast of Africa near 22°N, and by 29 July the center of maximum was found near 24°N, 40°W. (Note the leading concentration maximum depicted by the green shading near the Sargasso Sea "S" on this date, corresponding to the first simulated Fe concentration maximum depicted in Figure 6d.) On 31 July, two centers appear to be developing, one near 16°N, 60°W and another at 26°N, 58°W. Finally, on 2 August (Figure 13e), a distinct northern center (orange shading) is found, designated as the "event maximum," several hundred kilometers to the southwest of the cruise location S.

4.3.2.   Backward Trajectory Analysis

[48] The actual dust transport is three-dimensional. Dust storms over the Sahara produce a mix of all particle sizes extending from the surface up to levels as high as 500 mbar (~5.5 km). As the dust is transported westward away from the African source region, variable advection and wet scavenging alter the vertical distribution of dust, while particle sedimentation affects its size distribution. However, measurements of observed dust sizes using instruments with inherent uncertainties [*Reid et al.*, 2003a] tend to show an unexpected lack of vertical stratification of particle size [*Reid et al.*, 2003b]. On the other hand, a modeling study of Saharan dust transport to the Caribbean [*Colarco et al.*, 2003] demonstrated that the monthly average dust mass concentration and layering were affected by particle settling and regional atmospheric subsidence.

[49] Lagrangian trajectories are commonly used to determine the origin of observed dust episodes. These trajectories depict air parcel pathways; however, as a result of sedimentation or wet scavenging, aerosols can move vertically downward relative to an air parcel. If gravitational settling influences the evolution of dust transport events, air parcel trajectories could be potentially misleading. Figure 14 depicts a height-longitude cross section of simulated mineral dust transport with and without sedimentation as it is transported across the Atlantic at 24°N, roughly corresponding to the east-west dust concentration maximum illustrated in Figure 13. The control simulation with all transport processes including sedimentation produces a dust maximum that sinks with time while concentration values decrease. When sedimentation is removed from the simulation, a noticeable change in the dust profile is apparent. The center of the dust mean mass is found at higher altitudes with concentrations a factor of ~1.5 larger. Under this scenario, unrealistic high values of simulated mineral dust concentration are produced when compared with observed values in the Sargasso Sea during cruise 2.

[50] On the basis of these observations, our trajectories are adjusted for settling. We use NCEP reanalysis horizontal winds and, to be consistent with the dynamics used to drive the actual Eulerian transport model, recompute the vertical velocity from the horizontal mass divergence and surface pressure tendency. The vertical velocity is then adjusted by the computed regional mass-mean sedimentation rate, which is ~0.2 cm s^{-1} or ~17 m d^{-1} in the subtropical Atlantic. This value, although relatively small, allows the dust parcel to
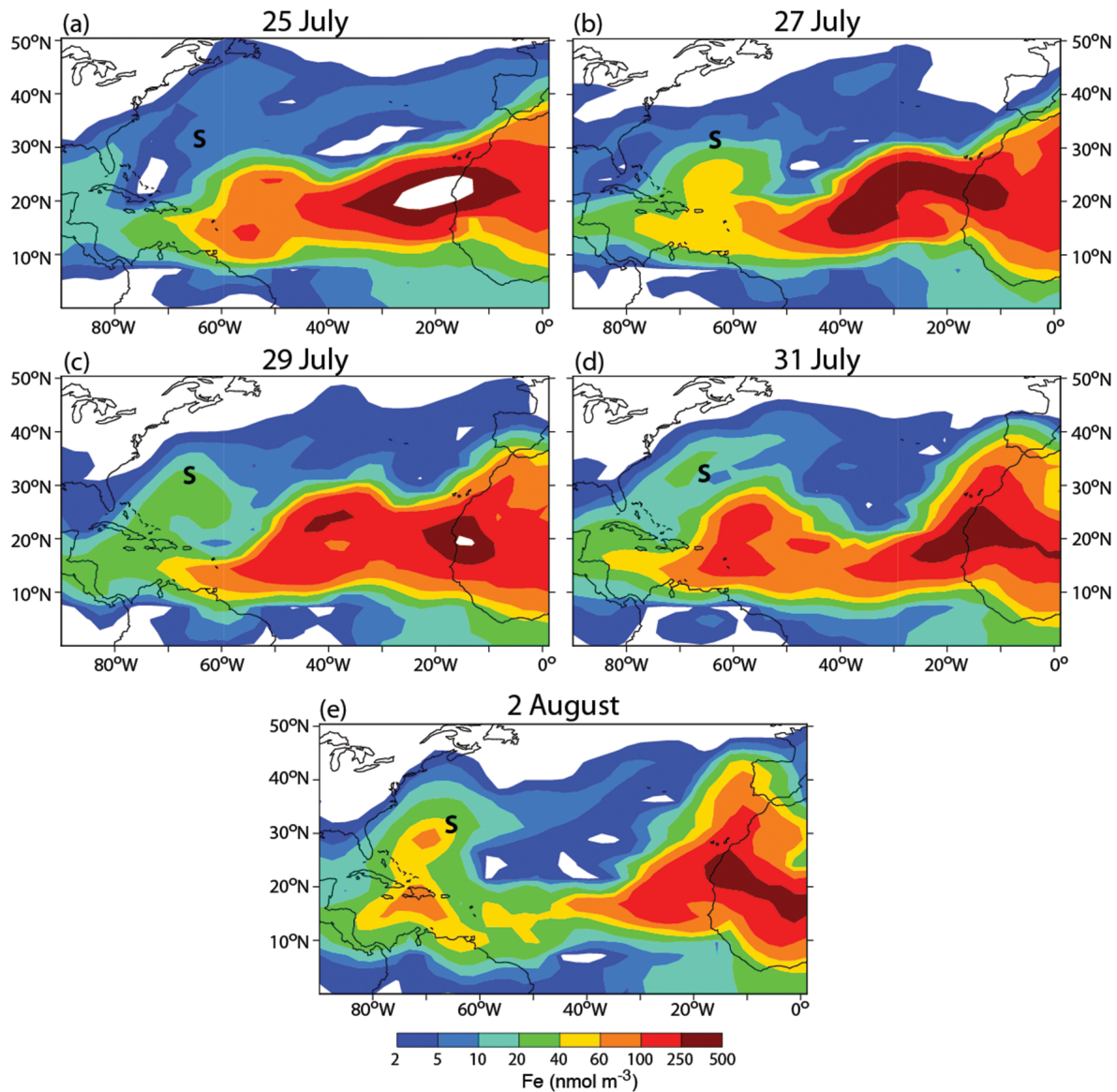
Figure 13. (a) Simulated mineral dust 850 mbar Fe concentrations (nmol m^{-3}) on 25 July 2003, and (b) 27 July, (c) 29 July, (d) 31 July, (e) and 2 August. Note that "S" represents the Sargasso Sea cruise 2 observation location.

experience different velocity and directional advection paths relative to the air parcel trajectory.

[51] An examination of mineral dust vertical profiles on 2 August revealed that the largest concentration of the event maximum occurred above the marine boundary layer near 900 mbar, while the greatest concentration of the cruise maximum located to the northeast was found at a somewhat higher level, 820 mbar. Consequently, 10-day back trajectories were computed for these two sites and starting altitudes (Figure 15a). The solid red line shows that the event maximum dust parcel begins in the deep mixed layer over the Sahara near 710 mbar and exits Africa to the west-northwest, arriving at a point west of the Canary Islands at 800 mbar on 28 July, where it merges with the location of the air parcel back-trajectory (blue dashed line) found at a lower altitude (860 mbar). The air parcel is shown to origi-

nate north of 40°N and travel southward anticyclonically under the influence of a strong high-pressure system near the Azores early in the period. From 28 July to 2 August, both the dust and air parcel travel the same directional path, an indication of the uniform flow around the subtropical high within the lower troposphere. The cruise maximum dust parcel trajectory (solid black line) begins at a higher level (640 mbar) over Africa and actually crosses over the event maximum trajectory around 29 July. The unadjusted air parcel pathway (not shown) originated at a lower altitude in Africa (~740 mbar); however, unlike the event maximum trajectory, there was essentially no directional separation, and the trajectory travels the same path at a lower altitude, arriving at 900 mbar on 2 August.

[52] To gain insight into the effect of directional shear, we first examine the average wind field over the Atlantic during
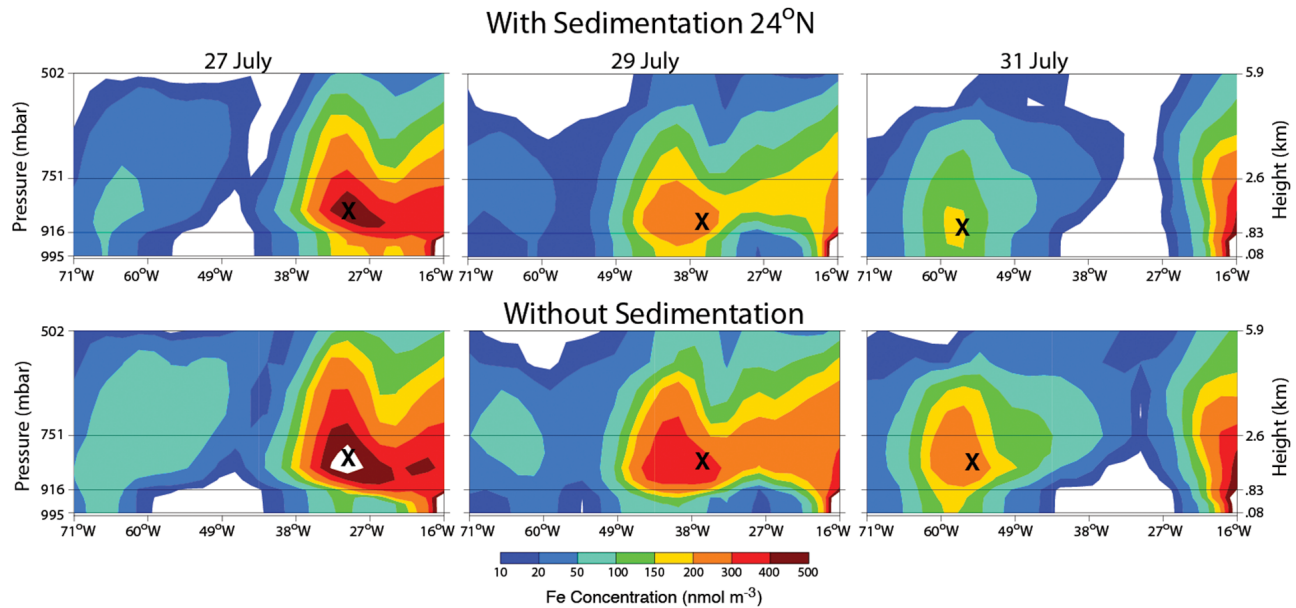
Figure 14. Height-longitude cross sections of mineral dust Fe concentrations (nmol m^{-3}) for 27 July 2003, 29 July 2003, and July 31 2003 at 28°N with sedimentation activated (top) and without sedimentation (bottom). Crosses indicate the approximate regions of maximum concentrations.

the timescale of the trajectories (~10 days) depicted in Figure 15b, where black heavy and light streamlines represent the 633 mbar wind field (~4 km) and the red and blue lines generalize the lower-level flow at 800 and 915 mbar, respectively. The dominant feature is the large anticyclonic circulation at 633 mbar that extends down to the surface (not shown) and encompasses most of the Atlantic. Also of interest is the col or neutral point (a region of weak winds and variable direction) located just to the west of the Canary Islands. We note that the event maximum trajectory leaves Africa under the influence of the col point and is drawn to the northwest while sinking and then comes under the control of anticyclonic flow at lower levels. In contrast, the cruise maximum trajectory leaves Africa farther to the south and at a higher altitude and consequently bypasses the col point region as it subsides on a general west-northwest course.

[53] The effect of the col region on the air parcel versus dust parcel separation becomes more apparent when we examine the streamline depiction on 26 July. The air parcel (indicated by A) is found at 850 mbar (Figure 16a) north of the col and resides in a strong northeast to southwest flow, while the dust parcel (indicated by D) at 750 mbar (Figure 16b) is located southwest of the col in a general southeast to northwest flow. With time, both parcels bypass the col point area and directionally merge downstream a few days later.

[54] The inconsistency between observational data and model simulation on the effects of settling remains to be resolved. However, this analysis of the Sargasso Sea dust event maximum provides evidence that the directional deviation of dust and air parcels in the subtropics is an intermittent and subtle process. In contrast, directional and vertical wind shear in midlatitudes can be strong during winter and spring, especially in relation to synoptic scale

cyclones. This would suggest a more significant separation of air parcel and dust parcel trajectories when analyzing long-range transport associated with Asian dust storm events.

4.3.3. SFeD

[55] The regional SFeD generated during the cruise period is also an intricate process. In nature, SFeD is produced by surface dry deposition of dust aerosols as well as by in-cloud and below-cloud scavenging of dust particles in rain events. Model simulations generate essentially continuous data at all grid boxes, allowing an unraveling of interdependent removal processes, while observational estimates of the dry SFeD as well as approximations of wet SFeD from the measured rate of precipitation and soluble Fe concentrations in rainwater are very sparse in space and noncontinuous in time. As an illustration of the complex day-to-day variations of SFeD, we reexamine the simulated SFeD for the Sargasso Sea cruise during the period from 24 July to 6 August 2003. Figures 17a and 17b compare the daily total Fe and soluble Fe concentrations within the model surface dust layer (995 mbar) in relationship to the SFeD (Figure 17c). Figures 17d–17f provide appropriate daily vertical profiles of soluble Fe concentrations, which determine the amount of SFeD during precipitation events. (Note that all soluble Fe concentrations in Figure 17 have been multiplied by 10 for plotting purposes.)

[56] One might assume that variations in total Fe concentrations would be a good indicator of variations in SFeD. However, upon examining the daily SFeD and total Fe concentrations in the surface dust layer (Figure 17a), it is apparent that the latter is not a good predictor of the former. The reasons are twofold: (1) Soluble Fe concentration also depends on the simulated solubility of aerosol Fe (Figure 17b), which itself depends on the history of chemical and cloud processing as well as dry and wet removal during transport
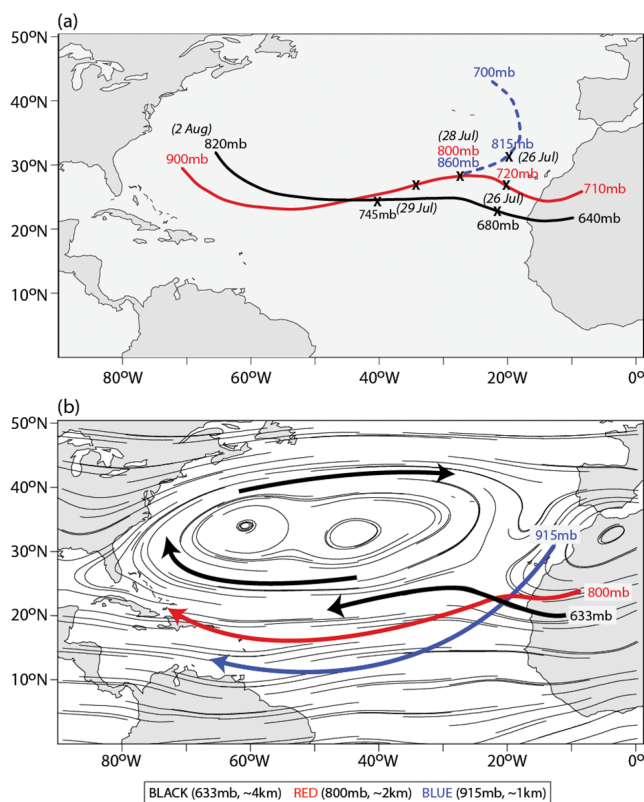
boundary layer (Figure 17e). The largest SFeD during the period was produced on 5 August, when high dust concentration (Figure 17a), coupled with high aerosol Fe solubilities at the surface and aloft (Figure 17f), produced a large soluble Fe concentration (Figure 17b), which was coincident with a significant rain event (Figure 17c).

5. Regional SFeD Rates: Monthly Mean Versus Daily

[58] It has been shown that the daily variability of mineral dust deposition within 1 month is much larger than the variability in monthly means over different years [*Mahowald et al.*, 2003; *Aumont et al.*, 2008]. Also, the observed and modeled episodic nature of surface dust concentrations and deposition, as well as the simulated daily SFeD in the
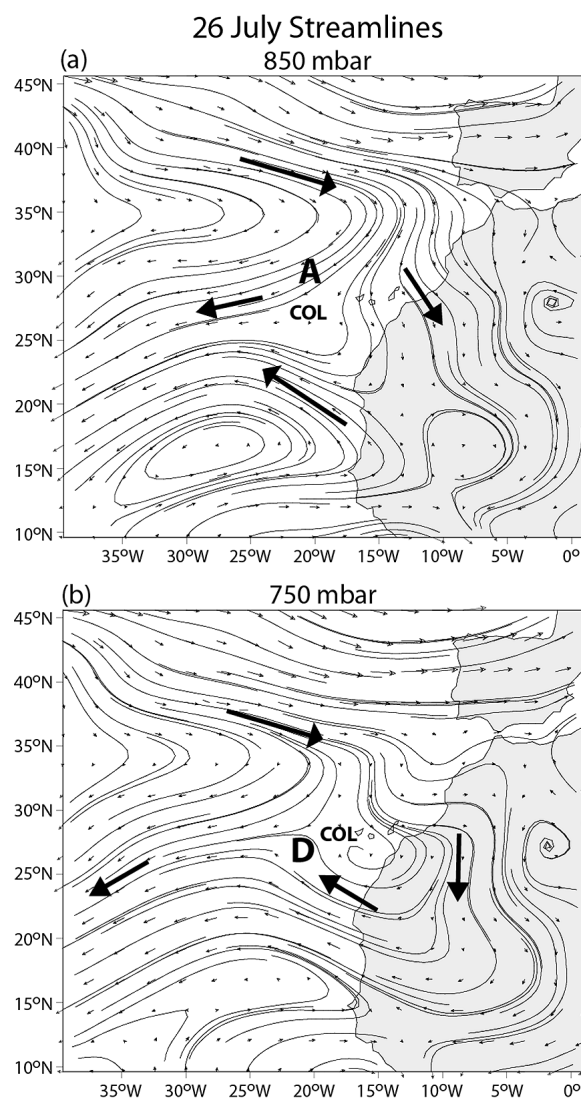

Figure 15. (a) Backward trajectories from 2 August 2003 to 23 July 2003 for the cruise measurement location (31°N, 64°W) at 820 mbar (black line) and the event maximum at 900 mbar (red line). The crosses mark the location corresponding to the labeled date and height (mbar). The dashed blue line represents the event maximum trajectory not adjusted for gravitational settling of dust. (b) Streamline flow field averaged over 23 July 2003 to 2 August 2003. The light black lines depict the streamline flow at the highest level (633 mbar, ~4 km), the heavy black line emphasizes the flow, the heavy red line depicts the general lower-level flow (800 mbar ~2 km), and the heavy blue line indicates the general flow at the lowest presented level (915 mbar, ~1 km).

from North Africa to the Sargasso Sea; and (2) precipitation events during the cruise produce SFeD that is a function of the vertical distribution of soluble Fe concentrations and is usually greater than surface dry deposition, which is solely dependent on surface concentrations (Figure 17c).

[57] The nature of this can be seen by examining shorter time period segments. From 29 July to 31 July, high total Fe concentrations correspond to relatively low soluble Fe concentrations because of low solubilities at the surface and aloft during this period (Figure 17d; 30 July). This, combined with the rain rate (not shown), has resulted in an intermediate SFeD in comparison to other days. From 2 August to 4 August, high total Fe and soluble Fe surface concentrations are favorable to dry deposition of SFeD, but lack of precipitation has resulted in small or zero wet SFeD. In contrast, large SFeD occurred on 1 August because of a rain event at a time when the soluble Fe concentration was low near the surface but sharply increased above the marine

Figure 16. Streamline flow field on 26 July 2003 for (a) 850 mbar where A represents the location of the air parcel trajectory. (b) 750 mbar where D represents the location of the dust parcel trajectory. Note COL represents a region of weak winds and variable direction known as a col or saddle point.
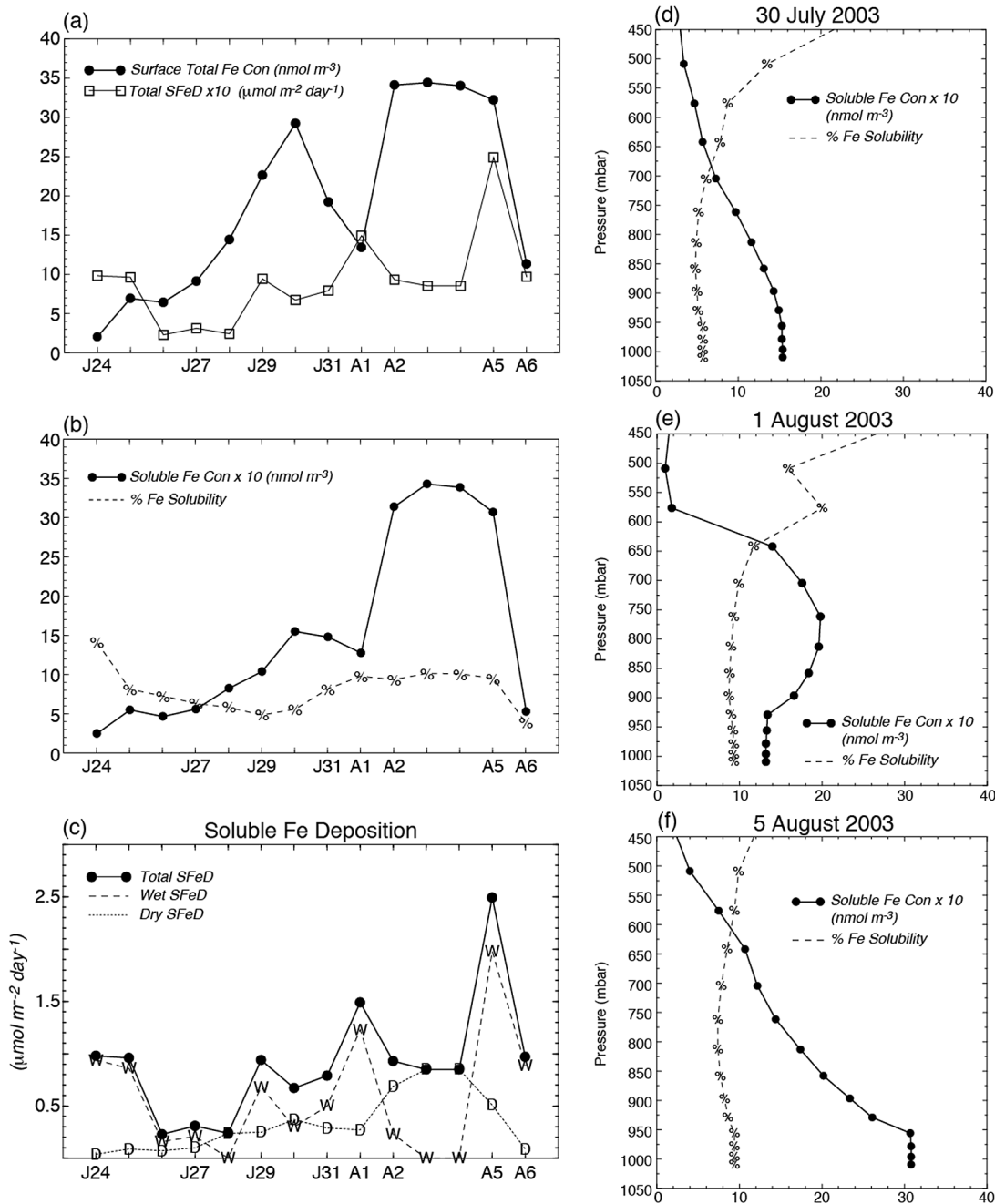
Figure 17. (a) Daily surface (995 mbar) time series (24 July 2003 to 6 August 2003) of mineral dust total Fe concentrations (nmol m^{-3}) (filled circles plotted on solid black line) and soluble Fe total deposition (SFeD) (μmol m^{-2} d^{-1}) multiplied by 10 (open squares plotted on black line). (b) Daily surface (995 mbar) time series of soluble Fe concentrations (nmol m^{-3}) multiplied by 10 (filled circles plotted on solid black line) and percentage soluble Fe plotted with % symbols. (c) Daily SFeD time series (μmol m^{-2} d^{-1}) of total flux (filled circles plotted on solid black line), wet flux (W plotted on dashed line), and dry surface flux (D plotted on dotted line). (d) Vertical profile on 30 July 2003 of soluble Fe concentrations (nmol m^{-3}) multiplied by 10 (filled circles plotted on solid black line) and percentage soluble Fe plotted with %. (e) Same as in Figure 17d for 1 August. (f) Same as in Figure 17d for 5 August 2003.

summer Sargasso Sea, all provide evidence that local synoptic scale SFeD events may be greater than the mean monthly flux rate. Ocean biogeochemical models, however, have typically adjusted their iron cycling on the basis of monthly climatological atmospheric deposition of mineral dust and an assumed constant Fe solubility. This masks effects from short-term bursts of SFeD that may influence phytoplankton uptake of excess Fe during periods of high
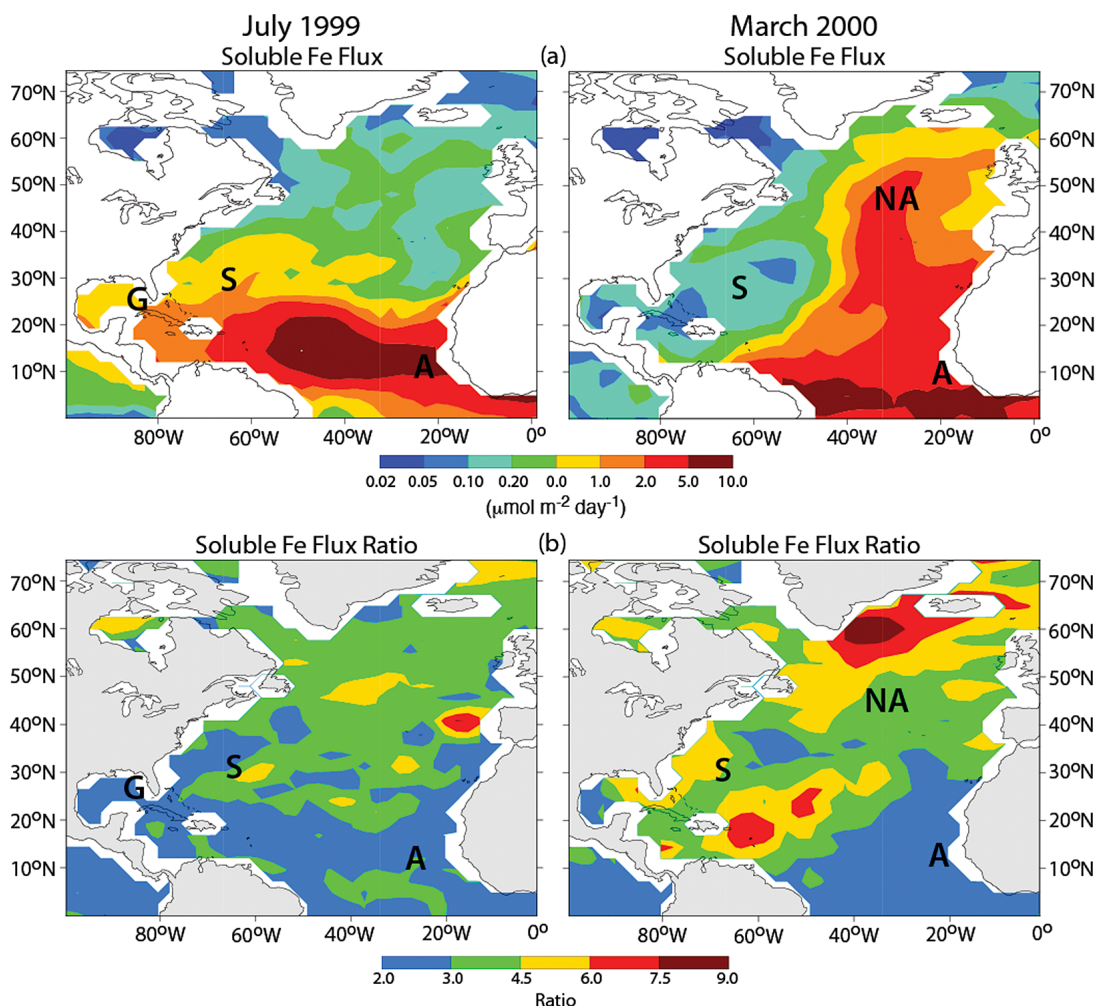
Figure 18. (a) SFeD (μmol m^{-2} d^{-1}) for July 1999 and March 2000. (b) Ratio of the average "high three" 1-d soluble Fe flux events to the monthly average rate. Note that locations A, S, G, and NA correspond to model time series sites shown in Figure 19.

availability [*Sunda and Huntsman*, 1995; *Kustka et al.*, 2003; *Jickells et al.*, 2005], as well as bloom initiation and magnitude [*Moore et al.*, 2006].

[59] To get a regional sense of the relative contrast of the monthly mean versus shorter timescale SFeD produced by mineral dust outbreaks, we present the monthly mean SFeD (Figure 18a) as well as the ratio of the average three largest daily SFeD events (high 3 flux (H3FLX), representing the high 10th percentile) to the monthly mean flux (MMF) (Figure 18b) during the months of July 1999 and March 2000. March 2000 was chosen because it represents the largest monthly springtime SFeD in the northeast Atlantic during our 13-year integration and was previously discussed, while July 1999 depicts a typical summer month. Within the region of maximum SFeD, H3FLX is a factor of 2 higher than the MMF during both months, while elsewhere ratios increase with decreasing MMF (larger than 4.5 during July and greater than 6 in March).

[60] To examine the diverse nature of simulated strong SFeD episodes, Figure 19 presents selected local daily time series for the months of July 1999 (Figure 19, left) and March 2000 (Figure 19, right). The grid box locations

indicated on Figures 18a and 18b are represented by the following letters: A (15°N, 25°W), S (Sargasso Sea), G (Gulf of Mexico), and NA (North Atlantic). During July off the coast of Africa (A), near the Sahara source region, there are five distinct pulses of SFeD (up to 14 μmol m^{-2} d^{-1}) associated with intermittent dust outbreaks and wet removal in the Intertropical Convergence Zone (ITCZ). In March, however, the same location now lies north of the ITCZ precipitation maxima and SFeD is controlled by comparatively slowly evolving surface dry removal containing two broad lower magnitude peaks. In the Sargasso Sea (S), July and March exhibit three large general episodes dominated by wet removal and three daily events more than three times larger than the MMF. However, the July MMF is nearly a factor of 6 times higher than March as a result of the prevailing climatological large summer mineral dust transport regime.

[61] During July 1999, a *Trichodesmium* bloom was observed in the southeastern Gulf of Mexico [*Lenes et al.*, 2001]. The bloom was conjectured to be associated with several concurrent Saharan mineral dust concentration events observed in Miami (see Figure 3b). The simulated time
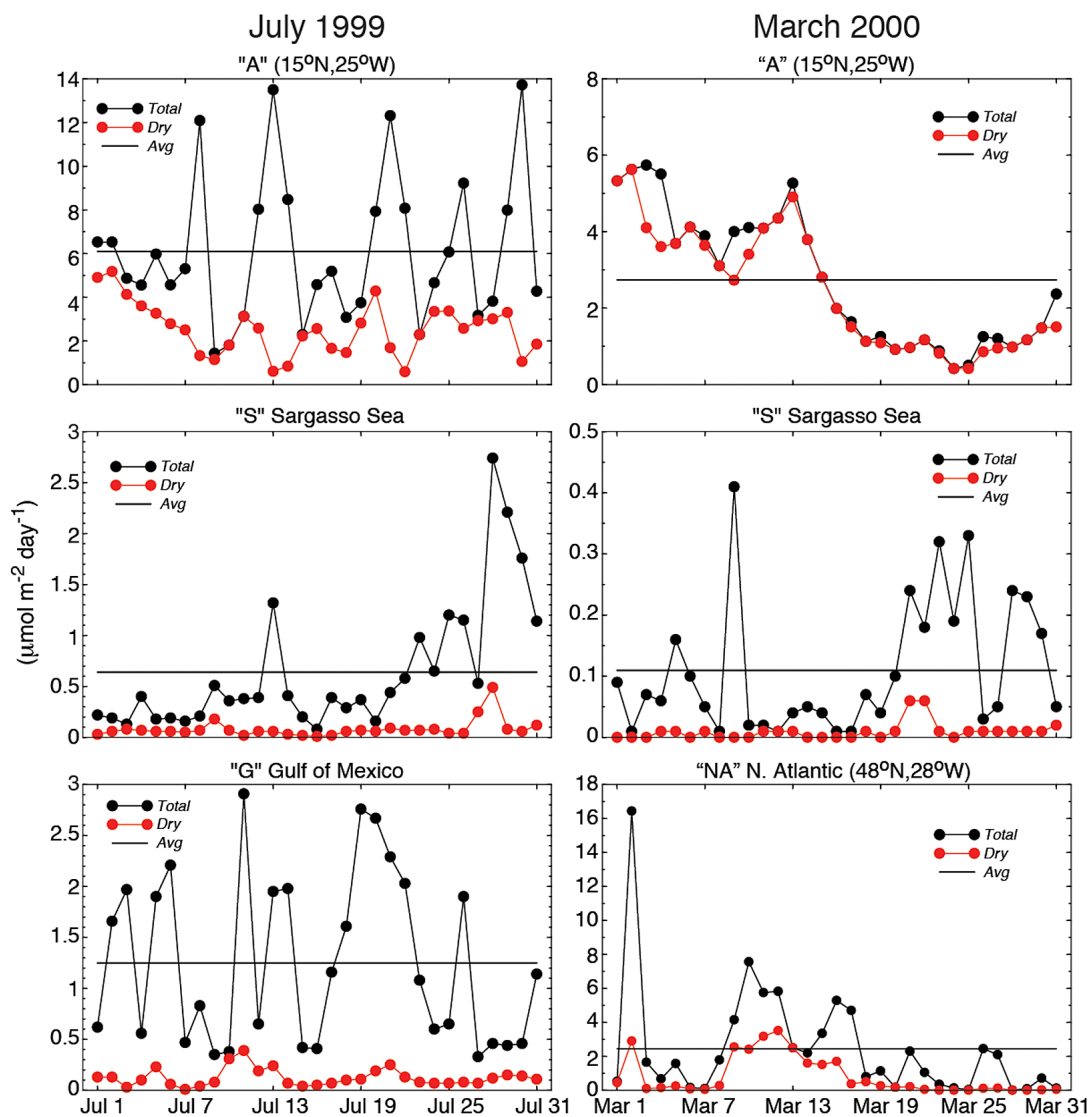
Figure 19. Selected monthly SFeD (μmol m^{-2} d^{-1}) time series sites for (left) July 1999 and (right) March 2000 for locations depicted in Figures 18a and 18b as A for off the west coast of Africa (15°N,25°W), S for Sargasso Sea, G for Gulf of Mexico, and NA for North Atlantic, displayed as total deposition (filled circles plotted on solid black line), dry deposition (filled red circles plotted on red line), and the mean deposition rate (straight black line). Note the different scales of SFeD magnitudes.

series in the Gulf of Mexico (G) shows that six pulses of wet removal SFeD occurred during this time with 3 days being more than a factor of 2 greater than the MMF, which could provide periods of high soluble Fe availability in the surface mixed layer.

[62] The work by *Moore et al.* [2006] hypothesized that Fe provided by episodic mineral dust deposition can influence the initiation, duration, and magnitude of the North Atlantic spring bloom. Keeping in mind that we have shown that this region experiences an extreme range of SFeD, from near zero to very large values, time series NA provides a look at the nature of prebloom March 2000 SFeD in the North Atlantic during the largest regional deposition month of this study, highlighted by three significant events. On 1 March, a huge event (16.5 μmol m^{-2} d^{-1}) is depicted, 6.6 times greater than the MMF of 2.5 μmol m^{-2} d^{-1}, which

in itself is large and was a result of the major Saharan dust outbreak discussed in section 4.2. This 1-d precipitation removal SFeD event is also larger in magnitude than events found at A just off the coast of Africa in July. To put this in perspective, an iron fertilization experiment in the equatorial Pacific Ocean [*Coale et al.*, 1996] seeded an area ~75 km^2 with three daily injections of soluble Fe ranging from 112 to 225 kg. In comparison, the 1 March simulated SFeD would supply ~70 kg to an area of 75 km^2.

6. Summary and Conclusions

[63] We have utilized the GFDL GCTM 13-year dust and soluble iron simulation to examine the meteorology of the mineral dust transport and SFeD in the North Atlantic Ocean. The purpose here was to introduce the complicated

interactions of mineral dust transport, sedimentation rate, wet and dry deposition, and chemical processing of soluble iron pertaining to SFeD within the framework of meteorological weather systems on timescales ranging from seasonal to daily. Instead of a more general statistical approach, we chose to present specific time periods of mineral dust transport and SFeD episodes in detail. While the GCTM simulations of observed dust events are not perfect, the ones that agree well with measurements allow us to unravel the meteorological complexity of SFeD from the initial dust mobilization in the Sahara to the eventual deposition in the remote ocean. Moreover, it is important to realize that while the magnitude of simulated SFeD would change with different and improved soluble Fe parameterization schemes, the transport processes would remain the same and the relative ratios of long-term average to short-term flux rates would vary little.

[64] The GCTM compares qualitatively well with observed mineral dust concentration and deposition as well as available measurements of the soluble Fe fraction within the North Atlantic basin. Also, the model's cumulative variable solubility SFeD over time periods corresponding to data from two cruises [*Sedwick et al.*, 2005; *De Jong et al.*, 2007] agreed well with observed changes of dissolved Fe within a thermally stratified surface mixed layer, while a simulation using a constant 2% solubility produced a significant underestimation.

[65] The northeast Atlantic receives its maximum seasonal SFeD during spring and experiences large year-to-year variability (>45% up to 90%) associated with the NAO. Strong NAO+ years can result in very large amounts of SFeD during times when synoptic scale cyclones coincide with outbreaks of Saharan dust, while amounts can be negligible during strong NAO− years. In contrast, summer produces the largest SFeD over the rest of the North Atlantic Ocean, with low year-to-year variability (<30%) as a result of relatively steady anticyclonic flow around the Azores High. Nevertheless, analysis of a synoptic scale summer dust concentration and SFeD event in the Sargasso Sea was shown to have a complex transport history. An air parcel back-trajectory of this event indicated a nonplausible origin in the dust-free lower troposphere over the northeast Atlantic Ocean. Dust particles, however, experience gravitational settling as they are advected across the Atlantic, thereby encountering different directional and velocity transport paths relative to an air parcel. Trajectories incorporating the dust sedimentation rate into the air parcel dynamic vertical velocity revealed that the proper dust parcel origin was in the Saharan air layer (~4 km) over Africa.

[66] The August 2003 Fe concentration and SFeD event observed during cruise 2 was shown to be a result of a variety of transport and removal processes. Large surface concentrations of total Fe do not necessarily correspond with large SFeD as a result of the following: (1) Soluble Fe concentrations depend on the solubility of aerosol Fe, which subsequently depends on the history of chemical and cloud processing as well as the dry and wet removal during transport from North Africa to the Sargasso Sea; and (2) local occurrences of precipitation acting on the height profile of soluble Fe concentrations produce wet removal events that are usually greater than surface dry deposition.

[67] Ocean biogeochemical models have typically used simulated climatological monthly mineral dust deposition and an assumed constant solubility for their atmospheric iron forcing. This reduces the amount of soluble Fe reaching the remote model ocean. In addition, the intermittent short-term (days) iron squalls can be four to six times larger than steady long-term average rates and may regionally affect phytoplankton uptake of Fe during these periods of high availability, potentially influencing bloom initiation and magnitude.

References

Anderson, J. R., P. R. Buseck, and T. L. Patterson (1996), Characterization of the Bermuda tropospheric aerosol by combined individual-particle and bulk-aerosol analysis, *Atmos. Environ.*, *30*, 319–338.

Aumont, O., L. Bopp, and M. Schulz (2008), What does temporal variability in Aeolian dust deposition contribute to sea-surface iron and chlorophyll distributions?, *Geophys. Res. Lett.*, *35*, L07607, doi:10.1029/2007GL031131.

Baker, A. R., T. D. Jickells, M. Witt, and K. L. Linge (2006a), Trends in the solubility of iron, aluminium, manganese and phosphorus in aerosol collected over the Atlantic Ocean, *Mar. Chem.*, *98*, 43–58.

Baker, A. R., M. French, and L. Linge (2006b), Trends in aerosol nutrient solubility along a west-east transect of the Saharan dust plume, *Geophys. Res. Lett.*, *33*, L07805, doi:10.1029/2005GL024764.

Bory, A.-M., and P. P. Newton (2000), Transport of airborne lithogenic material down through the water column in two contrasting regions of the eastern subtropical North Atlantic Ocean, *Global Biogeochem. Cycles*, *14*(1), 297–315, doi:10.1029/1999GB900098.

Buck, C. S., W. M. Landing, J. A. Resing, and G. T. Lebon (2006), Aerosol iron and aluminum solubility in the northwest Pacific Ocean: Results from the 2002 IOC cruise, *Geochem. Geophys. Geosyst.*, *7*, Q04M07, doi:10.1029/2005GC000977.

Burpee, R. W. (1972), The origin and structure of easterly waves in the lower troposphere of North Africa, *J. Atmos. Sci.*, *29*, 77–90.

Campana, K. A., Y.-T. Hou, K. E. Mitchell, S.-K. Yang, and R. Cullather (1994), Improved diagnostic cloud parameterization in NMC's global model, paper presented at 10th Conference on Numerical Weather Prediction, Am. Meteorol. Soc., Portland, Oreg.

Cana, L. (2002), The Saharan dust episode of 26 February 2000 over the Canary archipelago: A synoptic overview, *Weather*, *57*, 385–389.

Carlson, T. N., and J. M. Prospero (1972), The large-scale movement of Saharan air outbreaks over the northern equatorial Atlantic, *J. Appl. Meteorol.*, *11*, 283–297.

Cassar, N., M. L. Bender, B. A. Barnett, S.-M. Fan, W. J. Moxim, H. Levy II, and B. Tilbrook (2008), The southern ocean biological response to Aeolian iron deposition, *Science*, *317*, 1067–1070.

Chen, Y., and R. L. Siefert (2004), Seasonal and spatial distribution and dry deposition fluxes of atmospheric total and labile iron over the tropical and subtropical North Atlantic Ocean, *J. Geophys. Res.*, *109*, D09305, doi:10.1029/2003JD003958.

Chiapello, I., and C. Moulin (2002), TOMS and METEOSAT satellite records of the variability of Saharan dust transport over the Atlantic during the last two decades (1979–1997), *Geophys. Res. Lett.*, *29*(8), 1176, doi:10.1029/2001GL013767.

Christian, J. R., M. A. Verschell, R. Murtugudde, A. J. Busalacchi, and C. R. McClain (2002), Biogeochemical modeling of the tropical Pacific Ocean. I: Seasonal and interannual variability, *Deep Sea Res., Part II*, *49*, 509–543.

Church, T. M., A. Véron, C. C. Patterson, D. Settle, Y. Erel, H. R. Maring, and A. R. Flegal (1990), Trace elements in the North Atlantic troposphere: Shipboard results of precipitation and aerosols, *Global Biogeochem. Cycles*, *4*(4), 431–443, doi:10.1029/GB004i004p00431.

Coale, K. H., et al. (1996), A massive phytoplankton bloom induced by an ecosystem-scale iron fertilization experiment in the equatorial Pacific Ocean, *Nature*, *383*, 495–501.

Colarco, P. R., et al. (2003), Saharan dust transport to the Caribbean during PRIDE: 2. Transport, vertical profiles, and deposition in simulations of in

situ and remote sensing observations, *J. Geophys. Res.*, *108*(D19), 8590, doi:10.1029/2002JD002659.

Colin, J. L., J. L. Jaffrezo, and J. M. Gros (1990), Solubility of major species in precipitation: Factors of variation, *Atmos. Environ., Part A*, *24*(3), 537–544.

Cwiertny, D. M., et al. (2008), Characterization and acid-mobilization study of iron-containing mineral dust source materials, *J. Geophys. Res.*, *113*, D05202, doi:10.1029/2007JD009332.

De Jong, J. T. M., M. Boye, M. D. Gelado-Caballero, K. R. Timmermans, M. J. W. Veldhuis, R. F. Nolting, C. M. G. van den Berg, and H. J. W. De Baar (2007), Inputs of iron, manganese and aluminium to the surface waters of the northeast Atlantic and the European continental shelf, *Mar. Chem.*, *107*, 120–142.

Dentener, F. J., G. R. Carmichael, Y. Zhang, J. Lelieveld, and P. J. Crutzen (1996), Role of mineral aerosol as a reactive surface in the global troposphere, *J. Geophys. Res.*, *101*(D17), 22,869–22,889, doi:10.1029/96JD01818.

Desboeufs, K. V., R. Losno, F. Yimeux, and S. Cholbi (1999), The pH-dependent dissolution of wind-transported Saharan dust, *J. Geophys. Res.*, *104*(D17), 21,287–21,299, doi:10.1029/1999JD900236.

Duce, R. A., and N. W. Tindale (1991), Atmospheric transport of iron and its deposition in the ocean, *Limnol. Oceanogr.*, *36*, 1715–1726.

Edwards, R., and P. Sedwick (2001), Iron in East Antarctic snow: Implications for atmospheric iron deposition and algal production in Antarctic waters, *Geophys. Res. Lett.*, *28*(20), 3907–3910, doi:10.1029/2001GL012867.

Falkowski, P. G., R. T. Barber, and V. Smetacek (1998), Biogeochemical controls and feedbacks on ocean primary production, *Science*, *281*, 200–206.

Fan, S.-M., L. W. Horowitz, H. Levy II, and W. J. Moxim (2004), Impact of air pollution on wet deposition of mineral dust aerosols, *Geophys. Res. Lett.*, *31*, L02104, doi:10.1029/2003GL018501.

Fan, S.-M., W. J. Moxim, and H. Levy (2006), Aeolian input of bioavailable iron to the ocean, *Geophys. Res. Lett.*, *33*, L07602, doi:10.1029/2005GL024852.

Fecan, F., B. Marticorena, and G. Bergametti (1999), Parameterization of the increase of the Aeolian erosion threshold wind friction velocity due to soil moisture for arid and semi-arid areas, *Ann. Geophys.*, *17*, 149–157.

Fung, I. Y., S. K. Meyn, I. Tegen, S. C. Doney, J. G. John, and K. B. Bishop (2000), Iron supply and demand in the upper ocean, *Global Biogeochem. Cycles*, *14*, 281–295, doi:10.1029/1999GB900059.

Gao, Y., and J. R. Anderson (2001), Characteristics of Chinese aerosols determined by individual-particle analysis, *J. Geophys. Res.*, *106*(D16), 18,037–18,045, doi:10.1029/2000JD900725.

Gao, Y., S.-M. Fan, and J. L. Sarmiento (2003), Aeolian iron input to the ocean through precipitation scavenging: A modeling perspective and its implication for natural iron fertilization in the ocean, *J. Geophys. Res.*, *108*(D7), 4221, doi:10.1029/2002JD002420.

Ginoux, P., M. Chin, I. Tegen, J. M. Prospero, B. Holben, O. Dubovik, and S.-J. Lin (2001), Sources and distributions of dust aerosols simulated with the GOCART model, *J. Geophys. Res.*, *106*, 20,255–20,273, doi:10.1029/2000JD000053.

Ginoux, P., J. M. Prospero, O. Torres, and M. Chin (2004), Long-term simulation of global dust distribution with the GOCART model: correlation with the North Atlantic oscillation, *Environ. Modell. Software*, *19*, 113–128.

Giorgi, F. (1986), A particle dry-deposition parameterization scheme for use in tracer transport models, *J. Geophys. Res.*, *91*(D9), 9794–9806, doi:10.1029/JD091iD09p09794.

Gregg, W. W., P. Ginoux, P. S. Schopf, and N. W. Casey (2003), Phytoplankton and iron: Validation of a global three-dimensional ocean biogeochemical model, *Deep Sea Res., Part II*, *50*, 3143–3169.

Guieu, C., et al. (1997), Atmospheric input of dissolved and particulate metals to the northwestern Mediterranean, *Deep Sea Res., Part II*, *44*, 655–674.

Hand, J. L., N. M. Mahowald, Y. Chen, R. L. Siefert, C. Luo, A. Subramaniam, and I. Fung (2004), Estimates of atmospheric processed soluble iron from observations and a global mineral aerosol model: Biogeochemical implications, *J. Geophys. Res.*, *109*, D17205, doi:10.1029/2004JD004574.

Heymsfield, A. J., and L. J. Donner (1990), A scheme for parameterizing ice-cloud water content in general circulation models, *J. Atmos. Sci.*, *47*, 1865–1877.

Horowitz, L., et al. (2003), A global simulation of tropospheric ozone and related tracers: Description and evaluation of MOZART, version 2, *J. Geophys. Res.*, *108*(D24), 4784, doi:10.1029/2002JD002853.

Huang, J., C. Zhang, and J. M. Prospero (2010), African dust outbreaks: A satellite perspective of temporal and spatial variability over the tropical

Atlantic Ocean, *J. Geophys. Res.*, *115*, D05202, doi:10.1029/2009JD012516.

Hurrell, J. H. (1995), Decadal trend in the North Atlantic oscillation: Regional temperatures and precipitation, *Science*, *269*, 676–679.

Jickells, T., et al. (2005), Global iron connections between dust, ocean biogeochemistry and climate, *Science*, *308*, 67–71.

Jones, C., N. Mahowald, and C. Luo (2003), The role of easterly waves on African desert dust transport, *J. Clim.*, *16*, 3617–3628.

Kalnay, E. (1996), The NCEP/NCAR 40-year reanalysis project, *Bull. Am. Meteorol. Soc.*, *77*, 437–471.

Karyampudi, V. M., et al. (1999), Validation of the Saharan dust plume conceptual model using Lidar, Meteosat, and ECMWF data, *Bull. Am. Meteorol. Soc.*, *80*, 1045–1075.

Kasibhatla, P. S., H. Levy II, W. J. Moxim, and W. L. Chameides (1991), The relative impact of stratospheric photochemical production on tropospheric NO_y levels: A model study, *J. Geophys. Res.*, *96*, 18,631–18,646, doi:10.1029/91JD01665.

Kerkweg, A., S. Wurzler, T. Eisen, and A. Bott (2003), On the cloud processing of aerosol particles: An entraining air-parcel model with two-dimensional spectral cloud microphysics and a new formulation of the collection kernel, *Q. J. R. Meteorol. Soc.*, *129*, 1–18.

Kieber, R. J., K. Williams, J. D. Willey, S. Skrabal, and G. B. Avery Jr. (2001), Iron speciation in coastal rainwater: Concentration and deposition to seawater, *Mar. Chem.*, *73*, 83–95.

Kieber, R. J., J. D. Willey, and G. B. Avery Jr. (2003), Temporal variability of rainwater iron speciation at the Bermuda Atlantic Time Series Station, *J. Geophys. Res.*, *108*(C8), 3277, doi:10.1029/2001JC001031.

Kim, G., and T. M. Church (2002), Wet deposition of trace elements and radon daughter systematics in the South and equatorial Atlantic atmosphere, *Global Biogeochem. Cycles*, *16*(3), 1046, doi:10.1029/2001GB001407.

Klein, S. A., and D. L. Hartmann (1993), The seasonal cycle of low stratiform clouds, *J. Clim.*, *6*, 1587–1606.

Kohfeld, K., and S. P. Harrison (2001), DIRTMAP: The geological record of dust, *Earth Sci. Rev.*, *54*, 81–114.

Kustka, A. B., S. A. Sañudo-Wilhelmy, E. J. Carpenter, and W. G. Sunda, (2003), Iron requirements for dinitrogen and ammonium supported growth in cultures of *Trichodesmium* (IMS 101): Comparison with nitrogen fixation rates and iron:carbon ratios of field populations, *Limnol. Oceanogr.*, *48*, 1869–1884.

Lafon, S., J. L. Rajot, S. C. Alfaro, and A. Gaudichet (2004), Quantification of iron oxides in desert aerosol, *Atmos. Environ.*, *38*, 1211–1218.

Laj, P., G. Ghermandi, R. Cecchi, V. Maggi, C. Riontino, S. Hong, J.-P. Candelone, and C. Boutron (1997), Distribution of Ca, Fe, K, and S between soluble and insoluble material in the Greenland Ice Core Project ice core, *J. Geophys. Res.*, *102*(C12), 26,615–26,623, doi:10.1029/96JC02660.

Lam, P. J., J. K. B. Bishop, C. C. Henning, M. A. Marcus, G. A. Waychunas, and I. Y. Fung (2006), Wintertime phytoplankton bloom in the subarctic Pacific supported by continental margin iron, *Global Biogeochem. Cycles*, *20*, GB1006, doi:10.1029/2005GB002557.

Lenes, J. M., J. M. Prospero, D. E. Bates, K. A. Fanning, and J. J. Walsh (2001), Iron fertilization and the *Trichodesmium* response on the West Florida shelf, *Limnol. Oceanogr.*, *46*(6), 1261–1277.

Levin, Z., E. Ganor, and V. Gladstein (1996), The effects of desert particles coated with sulfate on rain formation in the eastern Mediterranean, *J. Appl. Meteorol.*, *35*, 1511–1523.

Levy, H., II, J. D. Mahlman, and W. J. Moxim (1982), Tropospheric N_2O variability, *J. Geophys. Res.*, *87*(C4), 3061–3080, doi:10.1029/JC087iC04p03061.

Luo, C., N. Mahowald, and J. del Corral (2003), Sensitivity study of meteorological parameters on mineral aerosol mobilization, transport and distribution, *J. Geophys. Res.*, *108*(D15), 4447, doi:10.1029/2003JD003483.

Luo, C., N. M. Mahowald, N. Meskhidze, Y. Chen, R. L. Siefert, A. R. Baker, and A. M. Johansen (2005), Estimation of iron solubility from observations and a global aerosol model, *J. Geophys. Res.*, *110*, D23307, doi:10.1029/2005JD006059.

Luo, C., N. Mahowald, T. Bond, P. Y. Chuang, P. Artaxo, R. Siefert, Y. Chen, and J. Schauer (2008), Combustion iron distribution and deposition, *Global Biogeochem. Cycles*, *22*, GB1012, doi:10.1029/2007GB002964.

Mackie, D. S., P. W. Boyd, K. A. Hunter, and G. H. McTainsh (2005), Simulating the cloud processing of iron in Australian dust: pH and dust concentration, *Geophys. Res. Lett.*, *32*, L06809, doi:10.1029/2004GL022122.

Mahlman, J. D., and W. J. Moxim (1978), Tracer simulation in a global general circulation model: Results from a mid-latitude instantaneous source experiment, *J. Atmos. Sci.*, *35*, 1340–1374.

Mahowald, N., C. Luo, J. del Corral, and C. Zender (2003), Interannual variability in atmospheric mineral aerosols from a 22-year model simulation and observational data, *J. Geophys. Res.*, *108*(D12), 4352, doi:10.1029/2002JD002821.

Mahowald, N. M., A. R. Baker, G. Bergametti, N. Brooks, R. A. Duce, T. D. Jickells, N. Kubilay, J. M. Prospero, and I. Tegen (2005), Atmospheric global dust cycle and iron inputs to the ocean, *Global Biogeochem. Cycles*, *19*, GB4025, doi:10.1029/2004GB002402.

Mahowald, N., et al. (2009), Atmospheric iron deposition: Global distribution, variability, and human perturbations, *Annu. Rev. Marine. Sci.*, *1*, 245–278, doi:10.1146/annurev.marine.010908.163727.

Marticorena, B., and G. Bergametti (1995), Modeling the atmospheric dust cycle: 1. Design of a soil-derived dust emission scheme, *J. Geophys. Res.*, *100*, 16,415–16,430, doi:10.1029/95JD00690.

Martin, S. T. (2005), Precipitation and dissolution of iron and manganese oxides, in *Environmental Catalysis*, edited by V. H. Grassian, pp. 61–81, CRC Press, Boca Raton, Fla.

Meskhidze, N., W. L. Chameides, A. Nenes, and G. Chen (2003), Iron mobilization in mineral dust: Can anthropogenic SO_2 emissions affect ocean productivity?, *Geophys. Res. Lett.*, *30*(21), 2085, doi:10.1029/2003GL018035.

Moore, C. M., M. M. Mills, A. Milne, R. Langlois, E. P. Achterberg, K. Lochte, R. J. Geider, and J. La Roche (2006), Iron limits primary productivity during spring bloom development in the North Atlantic, *Global Change Biol.*, *12*, 626–634.

Moore, J. K., S. C. Doney, and K. Lindsay (2004), Upper ocean ecosystem dynamics and iron cycling in a global three-dimensional model, *Global Biogeochem. Cycles*, *18*, GB4028, doi:10.1029/2004GB002220.

Morel, F. M. M., and N. M. Price, (2003), The biogeochemical cycles of trace metals in the oceans, *Science*, *300*, 944–947.

Moulin, C., C. E. Lambert, F. Dulac, and U. Dayan (1997), Control of atmospheric export of dust from North Africa by the North Atlantic oscillation, *Nature*, *387*, 691–694.

Ott, S.-T., A. Ott, D. W. Martin, and J. A. Martin (1991), Analysis of a trans-Atlantic Saharan dust outbreak based on satellite and GATE data, *Mon. Weather Rev.*, *119*, 1832–1850.

Ozsoy, T., and A. C. Saydam (2001), Iron speciation in precipitation in the northeastern Mediterranean and its relationship with Sahara dust, *J. Atmos. Chem.*, *40*, 41–76.

Pérez-Marrero, J., O. Llinas, L. Marato, M. J. Rueda, and A. Cianca (2002), Saharan dust storms over the Canary Islands during winter 1998 as depicted from the advanced very high-resolution radiometer, *Deep Sea Res., Part II*, *49*, 3465–3479.

Prospero, J. M. (1996), Saharan dust transport over the North Atlantic Ocean and Mediterranean: An overview, in *The Impact of Desert Dust from Northern Africa Across the Mediterranean*, edited by S. Guerzoni and R. Chester, pp. 133–151, Kluwer Acad., Dordrecht, Netherlands.

Prospero, J. M. (1999), Long-term measurements of the transport of African mineral dust to the southeastern United States: Implications for regional air quality, *J. Geophys. Res.*, *104*, 15,917–15,927, doi:10.1029/1999JD900072.

Prospero, J. M., and T. N. Carlson (1972), Vertical and areal distribution of Saharan dust over the western equatorial North Atlantic Ocean, *J. Geophys. Res.*, *77*, 5255–5265, doi:10.1029/JC077i027p05255.

Prospero, J. M., and P. J. Lamb (2003), African droughts and dust transport to the Caribbean: Climate change implications, *Science*, *302*, 1024–1027.

Prospero, J. M., and W. L. Landing (2007), Long-term measurements of African dust deposition across the state of Florida: How well do models do?, paper presented at the XXIV Conference, Int. Union of Geod. and Geophys., Perugia, Italy.

Prospero, J. M., P. Ginoux, O. Torres, S. Nicholson, and T. E. Gill (2002), Environmental characterization of global sources of atmospheric soil dust identified with the NIMBUS 7 Total Ozone Mapping Spectrometer (TOMS) absorbing aerosol product, *Rev. Geophys.*, *40*(1), 1002, doi:10.1029/2000RG000095.

Prospero, J. M., W. M. Landing, and M. Schulz (2010), African dust deposition to Florida: Temporal and special variability and comparison to models, *J. Geophys. Res.*, *115*, D13304, doi:10.1029/2009JD012773.

Raupach, M. R., D. A. Gillette, and J. F. Leys (1993), The effect of roughness elements on wind erosion threshold, *J. Geophys. Res.*, *98*, 3023–3029, doi:10.1029/92JD01922.

Reid, J. S., et al. (2003a), Comparison of size and morphological measurements of coarse mode dust particles from Africa, *J. Geophys. Res.*, *108*(D19), 8593, doi:10.1029/2002JD002485.

Reid, J. S., et al. (2003b), Analysis of measurements of Saharan dust by airborne and ground-based remote sensing methods during the Puerto Rico Dust Experiment (PRIDE), *J. Geophys. Res.*, *108*(D19), 8586, doi:10.1029/2002JD002493.

Riemer, N., O. M. Doherty, and S. Hameed (2006), On the variability of African dust transport across the Atlantic, *Geophys. Res. Lett.*, *33*, L13814, doi:10.1029/2006GL026163.

Rogers, R. R., and M. K. Yau (1989), *A Short Course in Cloud Physics*, 3rd ed., 290 pp., Elsevier, New York.

Ryall, D. B., R. G. Derwent, A. J. Manning, A. L. Redington, J. Corden, W. Millington, P. G. Simmonds, S. O'Doherty, N. Carslaw, and G. W. Fuller (2002), The origin of high particulate concentrations over the United Kingdom, March 2000, *Atmos. Environ.*, *36*, 1363–1378.

Sarthou, G., et al. (2003), Atmospheric iron deposition and sea-surface dissolved iron concentrations in the eastern Atlantic Ocean, *Deep Sea Res., Part I*, *50*, 1339–1352.

Sedwick, P. N., T. M. Church, A. R. Bowie, C. M. Marsay, S. J. Ussher, K. M. Achilles, P. J. Lethaby, R. J. Johnson, M. M. Sarin, and D. J. McGillicuddy (2005), Iron in the Sargasso Sea (Bermuda Atlantic Time-series Study region) during summer: Eolian imprint, spatiotemporal variability, and ecological implications, *Global Biogeochem. Cycles*, *19*, GB4006, doi:10.1029/2004GB002445.

Shi, Z., L. Shao, T. P. Jones, and S. Lu (2005), Microscopy and mineralogy of airborne particles collected during severe dust storm episodes in Beijing, China, *J. Geophys. Res.*, *110*, D01303, doi:10.1029/2004JD005073.

Siffert, C., and B. Sulzberger (1991), Light-induced dissolution of hematite in the presence of oxalate: A case study, *Langmuir*, *7*(8), 1625–1634.

Slingo, J. M. (1987), The development and verification of a cloud prediction model for the ECMWF model, *Q. J. R. Meteorol. Soc.*, *113*, 899–927.

Sunda, W., and S. Huntsman (1995), Iron uptake and growth limitation in oceanic and coastal phytoplankton, *Mar. Chem.*, *50*, 189–206.

Tegen, I., and I. Fung (1994), Modeling of mineral dust in the atmosphere: Sources, transport, and optical thickness, *J. Geophys. Res.*, *99*(D11), 22,897–22,914, doi:10.1029/94JD01928.

Tegen, I., S. P. Harrison, K. Kohfeld, I. C. Prentice, M. Coe, and M. Heimann (2002), Impact of vegetation and preferential source areas on global dust aerosol: Results from a model study, *J. Geophys. Res.*, *107*(D21), 4576, doi:10.1029/2001JD000963.

Torres-Padrón, M. E., M. D. Gelado-Caballero, C. Collado-Sanchez, V. F. Siruela-Matos, P. J. Cardona-Castellano, and J. J. Hernandez-Brito (2002), Variability of dust inputs to the CANIGO zone, *Deep Sea Res., Part II*, *49*, 3455–3464.

Trapp, J. M., F. J. Millero, and J. M. Prospero (2010), Trends in the solubility of iron in dust-dominated aerosols in the equatorial Atlantic trade winds: Importance of iron speciation and sources, *Geochem. Geophys. Geosyst.*, *11*, Q03014, doi:10.1029/2009GC002651.

Twohy, C. H., and J. R. Anderson (2008), Droplet nuclei in non-precipitating clouds: Composition and size matter, *Environ. Res. Lett.*, *3*, 045002, doi:10.1008/1748-9326/3/4/045002.

Twohy, C. H., et al. (2009), Saharan dust particles nucleate droplets in eastern Atlantic clouds, *Geophys. Res. Lett.*, *36*, L01807, doi:10.1029/2008GL035846.

Uematsu, M., R. A. Duce, and J. M. Prospero (1985), Deposition of atmospheric mineral particles in the North Pacific Ocean, *J. Atmos. Chem.*, *3*, 123–138.

Underwood, G. M., C. H. Song, M. Phadnis, G. R. Carmichael, and V. H. Grassian (2001), Heterogeneous reactions of NO_2 and HNO_3 on oxides and mineral dust: A combined laboratory and modeling study, *J. Geophys. Res.*, *106*(D16), 18,055–18,066.

Usher, C. R., A. Al-Hosney, S. Carlos-Cuellar, and V. H. Grassian (2002), A laboratory study of the heterogeneous uptake and oxidation of sulfur dioxide on mineral dust particles, *J. Geophys. Res.*, *107*(D23), 4713, doi:10.1029/2002JD002051.

Vichi, M., S. Masina, and A. Navarra (2007), A generalized model of pelagic biogeochemistry for the global ocean ecosystem. Part II: Numerical simulations, *J. Mar. Syst.*, *64*, 110–134.

Westbrook, C. D. (2008), The fall speeds of sub-100 μm ice crystals, *Q. J. R. Meteorol. Soc.*, *134*, 1243–1251.

Wong, S., P. R. Colarco, and A. E. Dessler (2006), Principal component analysis of the evolution of the Saharan air layer and dust transport: Comparisons between a model simulation and MODIS and AIRS retrievals, *J. Geophys. Res.*, *111*, D20109, doi:10.1029/2006JD007093.

Wurzler, S., T. G. Reisin, and Z. Levin (2000), Modification of mineral dust particles by cloud processing and subsequent effects on drop size distributions, *J. Geophys. Res.*, *105*(D4), 4501–4512.

Zender, C. S., H. Bian, and D. Newman (2003), Mineral Dust Entrainment and Deposition (DEAD) model: Description and 1990s dust climatology, *J. Geophys. Res.*, *108*(D14), 4416, doi:10.1029/2002JD002775.

Zhang, D., and R. A. Anthes (1982), A high-resolution model of the planetary boundary layer-Sensitivity tests and comparisons with SESAME-79 data, *J. Appl. Meteorol.*, *21*, 1594–1609.

Zhu, X. R., J. M. Prospero, and F. J. Millero (1997), Diel variability of soluble Fe(II) and soluble total Fe in North African dust in the trade winds at Barbados, *J. Geophys. Res.*, *102*(D17), 21,297–21,305, doi:10.1029/97JD01313.

Zhuang, G. S., Z. Yi, R. A. Duce, and P. R. Brown (1992a), Link between iron and sulphur cycles suggested by detection of Fe(II) in remote marine aerosols, *Nature*, *355*, 537–539.

Zhuang, G., Z. Yi, R. A. Duce, and P. R. Brown (1992b), Chemistry of iron in marine aerosols, *Global Biogeochem. Cycles*, *6*(2), 161–173, doi:10.1029/92GB00756.

S.-M. Fan, H. L. Levy II, and W. J. Moxim, Geophysical Fluid Dynamics Laboratory, NOAA, Princeton University, PO Box 308, 201 Forrestal Rd., Princeton, NJ 08540, USA. (bud.moxim@noaa.gov)